

1 **Fluvial reworking eliminates small craters, but does not**
2 **meaningfully bias the Mars interbedded-crater record**

3 **Andrew J. Moodie^{1,2}, Timothy A. Goudge^{2,3,4}**

4 ¹Department of Geography, Texas A&M University

5 ²Department of Earth and Planetary Sciences, Jackson School of Geosciences, The University of Texas at Austin

6 ³Center for Planetary Systems Habitability, The University of Texas at Austin

7 ⁴CIFAR Azrieli Global Scholars Program, CIFAR, Toronto, ON, Canada

8 **Key Points:**

- 9 • We simulated coeval river-delta and crater production, and quantified crater preservation in
10 resulting fluvial-deltaic stratigraphy
11 • Our findings indicate smaller craters are more often removed by fluvial reworking than larger
12 craters
13 • More smaller craters are produced than rivers can remove, bolstering some interpretations of
14 atmospheric paleo-pressure

15 THIS IS PREPRINT OF A RESEARCH ARTICLE SUBMITTED TO *Journal of Geo-*
16 *physical Research: Planets* ON 10/30/23. IT HAS NOT YET BEEN PEER RE-
17 VIEWED, OR ACCEPTED FOR PUBLICATION.

Corresponding author: Andrew J. Moodie, amoodie@tamu.edu

Abstract

Interpreting structures, morphology, and chemistry of the exposed stratigraphic record on Mars is complicated by ancient surface processes that variably removed parts of the record. Previous research has used the lack of smaller craters (≤ 50 m diameter) interbedded with fluvial deposits to constrain atmospheric pressure when rivers were active on Mars; the notion being that higher atmospheric pressure would have prevented smaller craters from forming. We hypothesize that contemporaneous channel lateral migration and avulsion could have reworked sedimentary deposits and eliminated craters from the stratigraphic record, thereby undermining atmospheric paleo-pressure interpretations. To test this hypothesis, we simulated coeval river-delta development and crater production, and quantified crater preservation in resulting stratigraphy. We document widespread crater degradation ($\sim 67\%$ of craters ≤ 50 m are at least partially eroded), and observe a marked increase in preservation with increasing crater diameter. That is to say, fluvial reworking preferentially removes smaller craters from the stratigraphic record. However, synthetic crater diameter distributions incorporating fluvial reworking effects do not reproduce observations on Mars, because so many smaller craters are produced and preserved. We find that, although river channels are sometimes in the right place to eliminate crater deposits from the stratigraphic record, production of smaller craters outpaces fluvial reworking under all modeled circumstances, and that a higher pressure ancient atmosphere is necessary to reproduce observations (i.e., consistent with existing interpretations of interbedded crater records). Our findings therefore bolster studies that assert fluvial reworking is not a primary control on smaller interbedded crater counts on Mars.

Plain Language Summary

Higher atmospheric pressure causes small impactors to break up before reaching the ground. So, researchers have used the lack of small craters observed over a specific time interval on Mars to infer what the atmospheric pressure was at that time interval. This has been particularly useful for early Mars, when water was thought to have been more abundant, implying the need for a thicker atmosphere. We hypothesized that another process, rivers migrating across the landscape, could preferentially remove small craters from the observable record, and would mislead researchers into thinking the lack of craters was due to high atmospheric pressure on ancient Mars. We tested our hypothesis with numerical modeling, and found that while our hypothesis is correct, migrating rivers cannot remove enough craters to explain the complete lack of small craters on Mars.

1 Introduction

Decades of research have leveraged the sedimentary structures, morphology, and chemistry of the exposed stratigraphic record on Mars to understand the evolution of the planet's ancient surface and atmosphere (e.g., Cabrol et al., 1999; Malin & Edgett, 2000; J. Grotzinger et al., 2005; Milliken et al., 2010; Cardenas et al., 2017; Goudge et al., 2018; Bishop et al., 2018; Day et al., 2019; Cardenas & Lamb, 2022). Of particular interest, is the formation timing of alluvial and lacustrine features on Mars, because these features likely demarcate the extent and duration of past hydrological activity that could have enabled life on the planet's surface (e.g., Bhattacharya, 2005). Without sample dating opportunities to date, absolute temporal constraints on formation of these features are determined by crater size-frequency distributions (CSFDs) paired with expected crater production rate models (i.e., crater counting; Hartmann, 1966; Hartmann & Neukum, 2001; Ivanov, 2001; Fassett, 2016). Interpreting crater records, and in particular those records from a planet with active sedimentary surface processes, is complicated by the interplay of ancient and modern surface processes that create, eliminate, and expose stratigraphic features (Jerolmack & Sadler, 2007; Kim

62 et al., 2014; Cardenas et al., 2022). For example, it is well known that modern surface processes can
63 readily degrade smaller craters ($\lesssim 50$ m) to the point the crater is unrecognizable (e.g., Hartmann,
64 1971; Fassett, 2016; Williams et al., 2018), and therefore bias the observed crater record. There
65 remains considerable uncertainty in how and under what circumstances the Mars crater record is bi-
66 ased by surface processes (Williams et al., 2018), and what the impact of this bias is on sedimentary
67 feature age estimates (M. Golombek et al., 2010).

68 The lack of smaller craters ($\lesssim 50$ m) embedded in the Mars stratigraphic record has been used
69 to constrain atmospheric paleo-pressure (e.g., Figure 1a; Kite et al., 2014; Warren et al., 2019).
70 These studies determine atmospheric pressure from crater sizes by assuming that there is a rela-
71 tionship between atmospheric pressure and the smallest size of impactors that can reach the planet
72 surface before complete ablation (e.g., higher atmospheric pressure raises the lower limit of possible
73 crater size; Popova et al., 2003; Williams et al., 2014). An additional assumption that atmospheric
74 ablation is the only significant process impacting crater size distributions, enables an inversion from
75 the measured CSFDs to atmospheric paleo-pressure, yielding an upper-bound pressure, in essence,
76 based on the *lack* of smaller craters. Kite et al. (2014) isolated craters interbedded with fluvial
77 deposits and that therefore formed when Mars rivers were active, and determined that the Mars
78 atmosphere would have been less than ~ 1.9 bar approximately 3.5 Ga. In another study using a
79 similar approach, Warren et al. (2019) found that Mars paleo-pressure was approximately 1.5 and
80 1.9 bar at 3.8 and 4 Ga, respectively (or oscillated around these values; Warren et al., 2019).

81 Atmospheric paleo-pressure interpretations are especially sensitive to identification of smaller
82 craters ($\lesssim 50$ m). Prior studies have examined preferential destruction of smaller craters due to wind-
83 blown erosion (Öpik, 1966; Hartmann & Neukum, 2001), diffusive down-slope transport driven
84 by subsequent impacts (Ross, 1968; Soderblom, 1970; A. Howard, 2004; Minton et al., 2015),
85 and flattening by seismic-shaking (Schultz & Gault, 1975; Richardson et al., 2004, 2005), as well
86 as covering by lava flows (Neukum & Horn, 1976; Hiesinger et al., 2002; Michael, 2013), and
87 obliteration during formation of new craters (i.e., saturation; Woronow, 1977, 1978; M. R. Smith
88 et al., 2008; Richardson, 2009; Minton et al., 2015). Other studies have discussed the potential for
89 erosion by fluvial processes to remove smaller craters (Irwin et al., 2013; Matsubara et al., 2018),
90 but this has not been examined in the context of craters that could become interbedded in a fluvial
91 sedimentary deposit (e.g., those craters in Kite et al., 2014). The potential impact of smaller crater
92 removal on paleo-pressure interpretations has not been rigorously evaluated.

93 River and delta activity is spatially and temporally heterogeneous, due to the movement of
94 channels across the landscape over time (Schumm, 1985; Straub et al., 2009). This channel move-
95 ment causes local fluctuations in deposition and erosion that create a stratigraphic record rife with
96 gaps and bias in recorded time (Sadler, 1981; Hajek & Straub, 2017; Straub et al., 2020). For
97 example, individual channel bends translate across the landscape eroding deposited material (e.g.,
98 Schumm, 1985), and leaving behind characteristic lateral accretion deposits, that are commensurate
99 in height to the channel depth (e.g., Figure 1b; Edwards & Eri, 1983; Bridge & Mackey, 1992). At
100 larger space and time scales, channels regularly relocate across the floodplain via avulsion, wherein
101 flow is steered across the landscape surface by topography and a new channel pathway is developed
102 (e.g., Frazier, 1967; Wells & Dorr, 1987; N. D. Smith et al., 1989; Hajek & Edmonds, 2014).

103 As a result of these channel movements, fluvial reworking of stratigraphy is scaled to a first
104 order by channel depth and channel mobility (Leeder, 1978; Ganti et al., 2011; Straub & Esposito,
105 2013; Wickert et al., 2013; Straub et al., 2015; Hajek & Straub, 2017). For example, a deeper
106 channel reaches farther into the subsurface and erodes sediment over a larger cross-sectional area,
107 and a more rapidly migrating or avulsing channel increases the proportion of the landscape visited

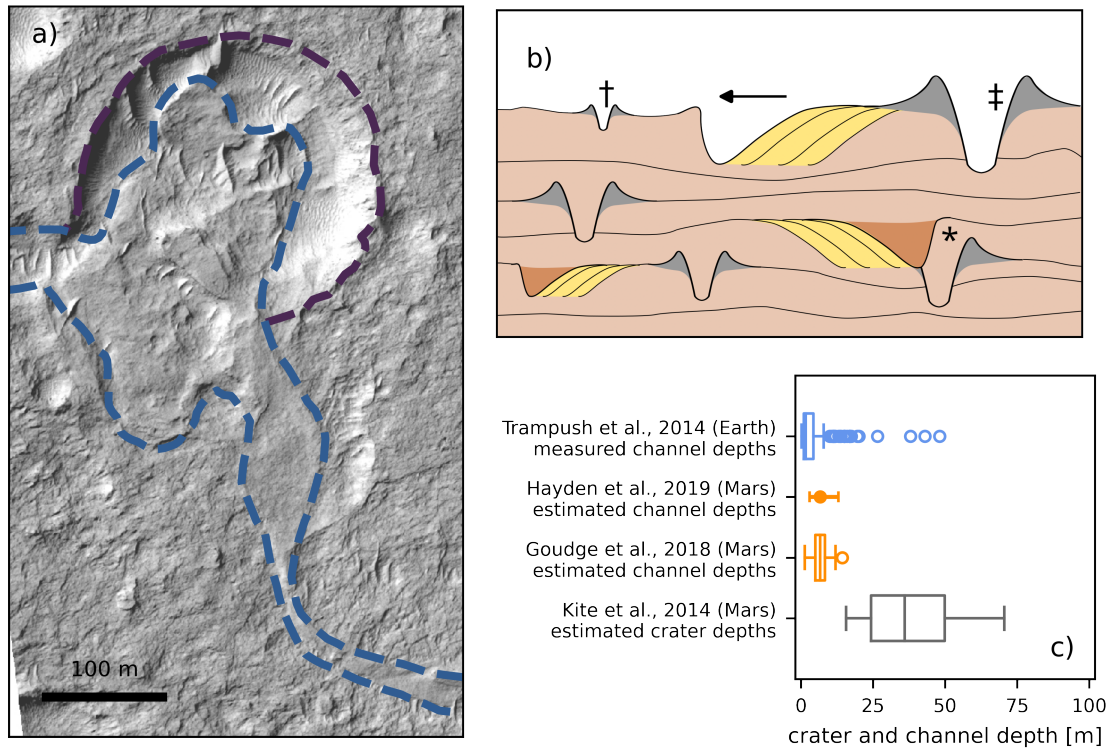


Figure 1. a) Example of a 238 m diameter crater (purple dashed line) interbedded with fluvial deposits (blue dashed lines) identified by Kite et al. (2013). Crater is located in the Aeolis Dorsa region, Mars (153.803E, 5.991S; HiRISE image ESP_017548_1740; NASA/JPL-Caltech/UArlizona; McEwen et al., 2007). b) Schematic cross-section of channel and crater interactions in the production of stratigraphy. The ← marks the migration direction of a channel located at the surface, which was steered by a larger crater marked by the ⊕. The † indicates a crater that may be removed from the record due to ongoing channel migration and the relative size of the channel and crater. In contrast, the larger crater (⊕) is unlikely to be removed, due to its position relative to the migration direction and larger size. In the stratigraphy, there are several fully preserved channel lateral migration deposits, and a crater rim that is partially preserved (marked by *), due to erosion by a migrating channel. c) Channel and crater depths on Earth and Mars (Trampush et al., 2014; Goudge et al., 2018; Hayden et al., 2019) have similar absolute scales to depths of craters missing from the ancient stratigraphic record on Mars, which has been used to estimate paleo-atmospheric pressure (Kite et al., 2014); here, a boxplot characterizes a distribution, and the solid circle and bar indicates a mean and range.

108 and where stratigraphy is destroyed. Moreover, whether a fluvial system is dominated by channel
 109 migration or avulsion is also known to affect stratigraphic reworking (Straub et al., 2009; Wang et
 110 al., 2011), with dominance between the two mobility modes being related to, among other factors,
 111 sediment composition (Straub et al., 2015; Liang et al., 2015a, 2016; Hajek & Straub, 2017). Finally,
 112 the fluvial system aggradation rate also affects stratigraphic reworking, because slower aggradation
 113 keeps sediments near the surface and within reach of channels for an increased duration (Hajek &
 114 Straub, 2017).

115 Coincidentally, typical river channel depths have similar absolute scales to smaller crater
 116 depths (Figure 1b,c). For example, typical alluvial river channel depths range 1–5 m on Earth
 117 (Trampush et al., 2014) and are estimated to have been 2–10 m on Mars (Goudge et al., 2018; Hay-

den et al., 2019), and crater depths range $<1\text{--}20$ m for craters $\lesssim 50$ m in diameter. Notably, initial crater depths of craters measured by Kite et al. (2014) would have been mostly deeper than estimated channel depths (Figure 1c), opening the possibility that the “missing” smaller craters were removed from the record by migrating river channels. Moreover, it is known that ancient channels moved across the Mars landscape when the stratigraphic interval of interest was produced (Goudge et al., 2018; Hayden et al., 2019; Cardenas & Lamb, 2022).

Overlapping absolute dimensions of fluvial channels and smaller craters raise the possibility that fluvial reworking has removed a substantial portion of smaller interbedded craters from the Mars stratigraphic record. Indeed, if fluvial reworking substantially biased the Mars crater record, the lack of smaller craters would not be a robust proxy for atmospheric paleo-pressure (Kite et al., 2014). Warren et al. (2019) applied an analytical size-dependent filter to approximate crater removal by sedimentary processes and investigate if these processes could meaningfully change paleo-pressure interpretations. Their study determined that the process-filter could not explain the observed Mars crater record, but the functional form and parameterization of the analytical filter were not calibrated or validated. We hypothesize that fluvial activity can rework and eliminate from the stratigraphic record crater deposits that form proximally to river channels (i.e., interbedded craters).

We further hypothesize that because smaller craters ($\lesssim 50$ m diameter) present a less significant physical obstacle to a laterally migrating or avulsing river than larger craters ($\sim 50\text{--}300$ m diameter), there is a crater size-dependent bias in the removal of craters by fluvial reworking. This preferential removal of smaller craters would adjust atmospheric paleo-pressure interpretations downwards, by confirming the possibility that unobserved crater diameters were eliminated by fluvial reworking, rather than by atmospheric ablation.

In this study, we answer the question: can fluvial reworking explain the lack of smaller interbedded craters ($\lesssim 50$ m) on Mars? We first forward modelled coeval river-delta evolution and crater production, and assessed preservation of craters within the fluvial-deltaic stratigraphy. With these observations, we studied how mappable crater size-frequency distributions are impacted by fluvial reworking, and determine how to account for this bias when making atmospheric paleo-pressure interpretations.

2 Modeling crater production and delta sedimentation

We simulated river-delta development with coeval crater production using open-source research software. We use Python 3.9.5 and *pyDeltaRCM* v2.1.4 for delta modeling (Moodie et al., 2021), and coupled it with crater size-frequency distributions generated with *craterstats2* v3.0.11 (Michael et al., 2016), and an analytical framework describing fresh crater geometries (A. D. Howard, 2007). Our workflow is fully reproducible, and all modeling and analysis codes are archived, with links to repositories in the Open Research Section.

2.1 Crater size-frequency distributions

The accumulated history of crater production and destruction is recorded in crater size-frequency distributions (CSFDs). Most commonly, a crater size-frequency distribution (CSFD) is measured over a control area and used to constrain surface age (e.g., Fassett, 2016). This approach compares the measured CSFD to modeled CSFDs that would be expected for surfaces with different ages, modeled CSFDs are made by combining an expected proportionality of craters of different sizes (a so-called “production function”) with a historical crater production rate (a so-called “chronology

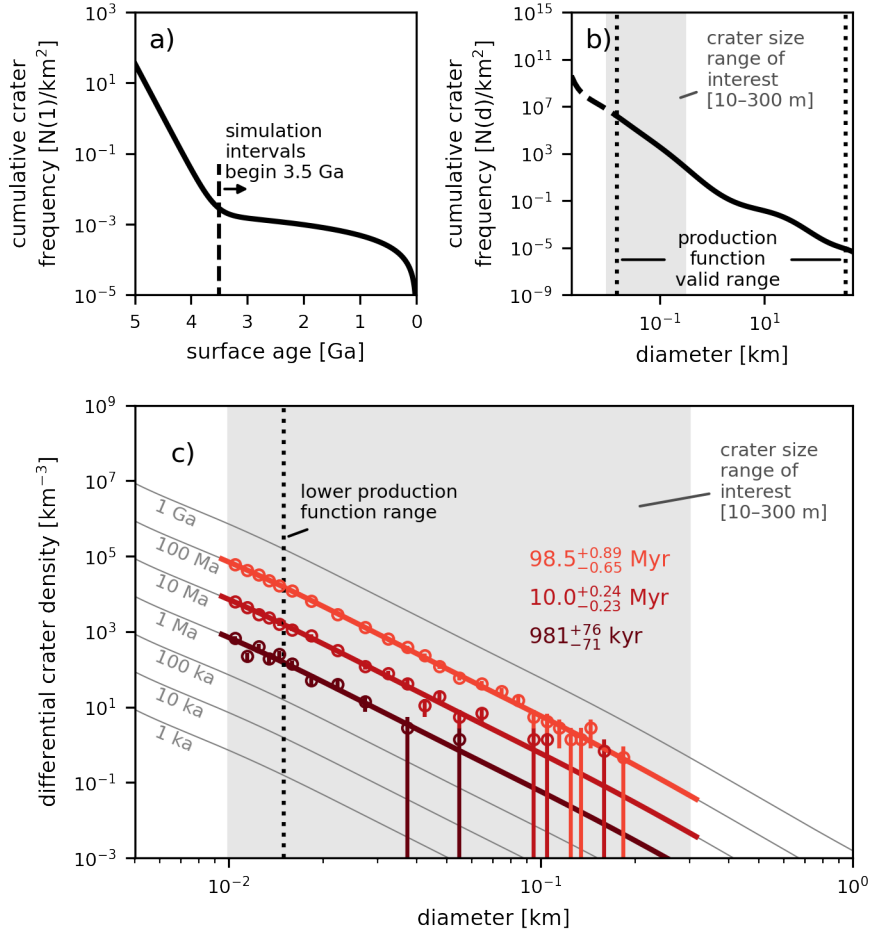


Figure 2. a) The Hartmann and Neukum (2001) Mars chronology function, describing the number of 1 km diameter craters per km², accumulated on a surface with a given age. b) The Ivanov (2001) Mars production function, describing the relative abundance of craters by diameter. c) The chronology function and production function are used together in a Monte Carlo simulation to generate crater-size populations representing time durations of 1 Ma, 10 Ma, and 100 Ma, and beginning 3.5 Ga, which are then used in model simulations (see text for additional details; Michael et al., 2016).

160 function”). Production and chronology functions are calibrated for the Moon, and are extended to
 161 other celestial bodies, including Mars (Ivanov, 2001).

162 We synthesized crater size-frequency distribution samples for our coupled delta-cratering
 163 model via Monte Carlo simulation, following the approach of Michael et al. (2016). We selected the
 164 Hartmann and Neukum (2001) Mars chronology function and Ivanov (2001) Mars production func-
 165 tion for simulation. Monte Carlo simulations begin during the era of vigorous hydrological activity
 166 on ancient Mars at 3.5 Ga (Fassett & Head, 2008; Hoke & Hynek, 2009; Mangold et al., 2012), and
 167 include craters in the diameter range 10–300 m. Notably, the lower bound of our crater size range
 168 of interest extends beyond the size range of our chosen production function (Figure 2b; Ivanov,
 169 2001); over this extrapolated diameter range, the slope of the production function is consistent with
 170 diameters within the function valid range (Figure 2b).

171 Monte Carlo simulation proceeds by choosing a crater size from a uniform probability distri-
172 bution over the size range of interest, and determining the instantaneous cratering rate for that crater
173 size from the chronology and production functions. The time to the next cratering event depends on
174 the selected crater size, such that over many crater iterations, the synthesized crater size-frequency
175 distribution conforms with the production function, and the distribution is consistent with a specified
176 amount of elapsed time (Figure 2c). We specify CSFDs that represent elapsed time of 1, 10, and
177 100 Myr for simulations (Figure 2c).

178 We limited crater production to diameters less than 300 m because larger features can generate
179 morphodynamic instability in the numerical delta model. We expect that this is a reasonable upper
180 bound for craters that may be partially reworked by fluvial activity, but are unlikely to be completely
181 eliminated from the stratigraphic record; this assumption will be tested with simulations.

182 2.2 Delta model

183 Coeval delta and crater production was simulated with the *pyDeltaRCM* numerical model
184 (Moodie et al., 2021), which is a flexible implementation of the widely used DeltaRCM delta model
185 (Liang et al., 2015a). DeltaRCM model design has been robustly validated (Liang et al., 2015a,
186 2015b, 2016) and used to examine delta morphology and evolution under various external forcings
187 and processes (Lauzon & Murray, 2018; Lauzon et al., 2019; Piliouras et al., 2021; Moodie &
188 Passalacqua, 2021; Hariharan et al., 2021, 2022, 2023). In this article, we do not describe the
189 complete model implementation, and instead provide a high-level overview that highlights model
190 components relevant to our study design and interpretations; a full model description is given in
191 Liang et al. (2015a).

192 In DeltaRCM, a deltaic landform emerges from rules that iteratively route water and sedi-
193 ment via weighted random walk, from a fixed inlet location and into an initially empty receiving
194 basin (Figure 3a; Liang et al., 2015a). Water is steered primarily by topographic gradients, moving
195 down-gradient, and sediment is routed according to topographic and hydrodynamic gradients, with
196 weighting that varies between the two for different sediments (Liang et al., 2015a; Wright et al.,
197 2022). The routing rules were developed with “just enough” complexity to yield realistic deltaic
198 channel dynamics, so that the model maintains simplicity and computational efficiency (Liang et
199 al., 2015a). Importantly, the dependence of water and sediment routing on topography is the fun-
200 damental connection between crater formation and delta formation; we did not modify any model
201 routing rules for this study, including modifications to the effect of gravity on sediment suspension
202 and transport (Supplementary Materials; e.g., Braat et al., 2023). DeltaRCM is known to be underes-
203 timate non-local and backwater hydrodynamic effects that develop upstream of channel bifurcations
204 and obstructions (Liang et al., 2015b). As a result, water and sediment are erroneously transported
205 up-slope in some uncommon circumstances where flow energy is especially high; in that case, high
206 topography outside of channels may be unrealistically lowered (Liang et al., 2015a). Nevertheless,
207 our modeling aims to capture the first-order effects of river and crater interactions, and so while
208 we recognize that these model limitations are present, we do not expect model idiosyncrasies to
209 significantly impact our results.

210 The mixture of sediment grain sizes input to a river delta is known to impact delta morphology
211 and dynamics (Edmonds & Slingerland, 2010), and this dependence is borne out in DeltaRCM as
212 well (Liang et al., 2015a, 2016; Hariharan et al., 2021; Moodie & Passalacqua, 2021). In DeltaRCM,
213 the sediment mixture is controlled by a “sand fraction” parameter that shifts the mixture from muddy
214 to sandy, and therefore transitions the delta between two modes of channel mobility. Channels in
215 muddy simulations are generally stable, exhibiting a single active channel with moderate local lat-

216 eral migration of channel bends, that is punctuated by large delta-scale lobe-switching avulsions
 217 that swiftly relocate the channel across the delta. In contrast, sandy simulations maintain multiple
 218 simultaneously-active channels that extensively migrate and frequently avulse across the landscape
 219 at multiple spatial scales (Liang et al., 2015a). Additionally, muddy simulations exhibit higher sur-
 220 face roughness, that is, higher average elevation variation across the landscape (Liang et al., 2016),
 221 which means that avulsions in muddy simulations develop new channels unevenly and in deep to-
 222 pographic lows, whereas avulsions in sandy simulations distribute sediment more evenly across
 223 the landscape. Importantly, this change in surface channel mobility translates to increased rework-
 224 ing of sedimentary deposits and stratigraphy for sandy simulations, relative to muddy simulations
 225 (Hariharan et al., 2021).

226 *pyDeltaRCM* uses a flow intermittency assumption to represent only morphodynamically ac-
 227 tive time, and therefore decrease model computation time. This common modeling assumption (e.g.,
 228 Parker, 2004) is based on the nonlinear relationship between water and sediment discharge, and the
 229 increasing rarity of flows of increasing magnitude (Wolman & Miller, 1960). In essence, there is
 230 a river discharge that moves significant sediment volumes and occurs frequently, such that this dis-
 231 charge is treated as the meaningful control on the long-term evolution of the landform; only this
 232 discharge is modeled and is scaled to represent elapsed total time. Flow intermittency on Mars is
 233 poorly constrained (Stucky de Quay et al., 2021; Buhler et al., 2014), so model design simply as-
 234 sumes that significant flow intervals are evenly distributed over the duration of the simulation (e.g.,
 235 not randomly distributed, but divided evenly over 100 Myr of elapsed total time).

236 In our simulations, water and sediment debouch into the 6 m deep receiving basin from a 6 m
 237 deep and 150 m wide channel at 1,350 m³/s and 1.35 m³/s discharge, respectively. The model uses
 238 a grid spacing of 20 m, over a 6×12 km domain. Simulations use a moderate sediment composition
 239 value, with equal parts sand and mud (i.e., sand fraction value is 0.5), which is within the broad range
 240 of grain size mixtures observed on Earth and Mars (J. P. Grotzinger et al., 2015; Stack-Morgan et al.,
 241 2023). These simulation parameters lead to development of channels 118 ± 68 m wide and 7 ± 3 m
 242 deep that exhibit dynamics consistent with real-world systems (Liang et al., 2015a, 2016). We ran
 243 simulations for 10,000 timesteps, which amounts to 107×10⁶ seconds of intermittent bankfull river
 244 flow. At the end of the simulation, deposits extend 4–5 km into the basin and span 8–10 km per-
 245 pendicular to the inlet channel (Figure 3e), therefore maintaining an approximately axis-symmetric
 246 planform over many cycles of channel movement (Parker et al., 1998; Reitz & Jerolmack, 2012;
 247 Moodie et al., 2019).

248 The model domain size and initial configuration, with a flat basin and single narrow inlet
 249 (Figure 3a) is conceptually consistent with a delta forming on the floor of a large crater (>30 km
 250 diameter) from an inlet valley cutting across the crater rim. Notably, delta deposits at the end of
 251 simulation (Figure 3e) scale similarly to the Jezero Crater western delta deposits (e.g., Fassett &
 252 Head III, 2005; Goudge et al., 2018), though we did not explicitly attempt to model these deposits.

253 **2.3 Coupling cratering and the delta model**

254 Before beginning a simulation, we generate a crater-size distribution commensurate to the
 255 timescale of interest (e.g., 100 Myr) and determine independent crater formation times (i.e., cratering
 256 is a random Poisson process Herkenhoff & Plaut, 2000; Michael et al., 2016). Craters are placed
 257 between delta-model timesteps (Figure 3a–e), and are located randomly within the model domain but
 258 rectified to the model grid. Fresh crater geometry is generated according to (A. D. Howard, 2007),
 259 with the modification that ejecta deposits are not modeled beyond 6× the crater radius. Crater
 260 formation is instantaneous, and has no effect on sediment erodibility in the delta model. Craters

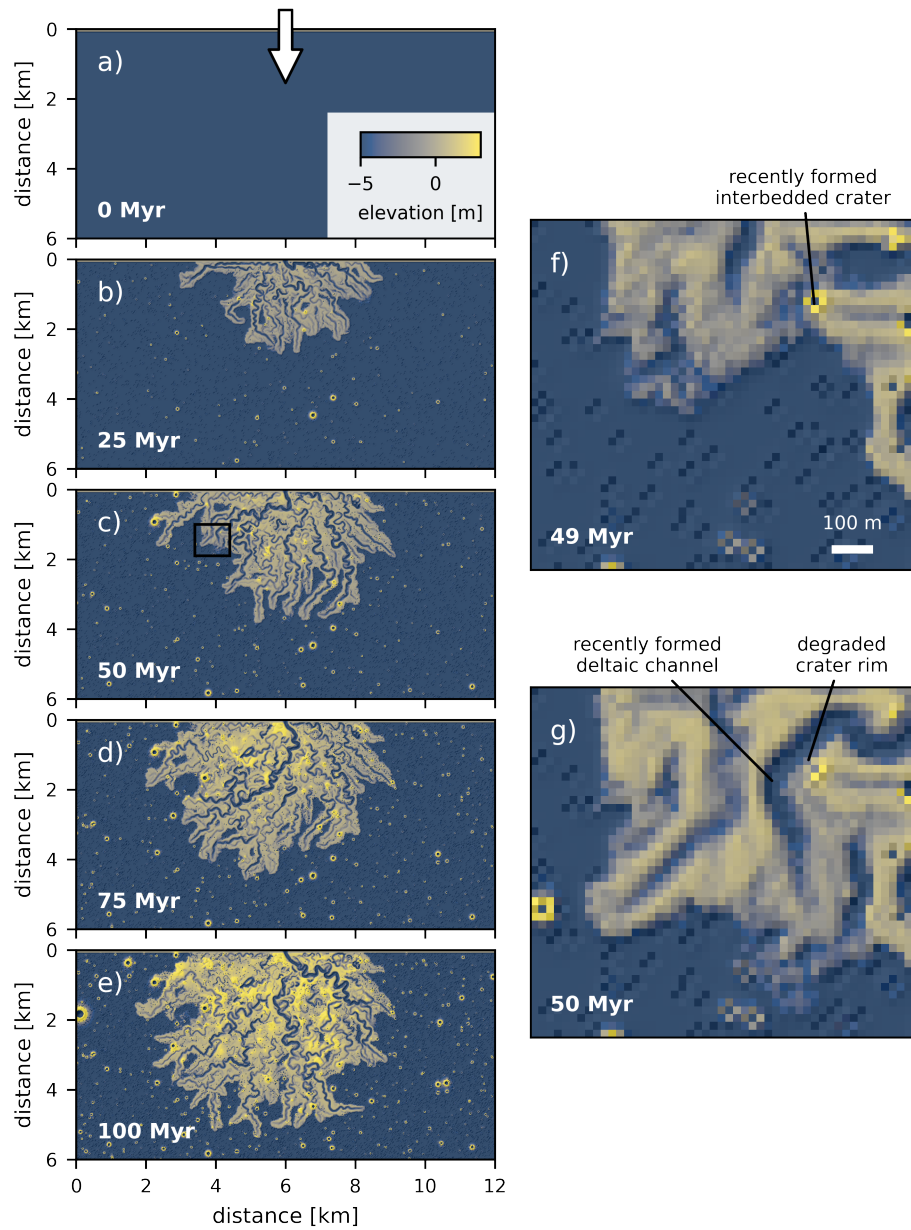


Figure 3. a–e) Timeseries of coeval river-delta and crater production for one 100 Myr simulation; color from blue to yellow highlights delta elevation. f–g) Highlight from timeseries at 49 to 50 Myr, showing a fluvial channel formed via avulsion and the associated partial degradation of an older crater ~ 20 m in diameter; location of highlighted area is shown by black square in panel c.

261 $\lesssim 30$ m have shorter rim heights in our model than predicted by A. D. Howard (2007) geometric
 262 rules, due to grid discretization effects (Supplementary Materials). This may artificially increase the
 263 ability of smaller modeled craters ($\lesssim 30$ m) to be removed, versus larger craters; though, in either
 264 case rim elevations are < 10 m and a similar scale to channel depths.

265 Each crater rim and ejecta deposit is tagged with a unique identifier, so that these materials
 266 are identifiable in the final modeled stratigraphy (Figure 4b). Rim material is labeled from $0.9r \leq$
 267 $x < 1.41r$, where r the crater radius and x is distance from the crater center, and crater ejecta is
 268 labeled from from $1.41r \leq x \leq 6r$. A single exception is that a minimum one-cell-wide annulus is
 269 created around a minimum one-cell central crater-floor cell; i.e., for the smallest craters, there is
 270 a single crater-floor cell with the eight surrounding neighbor cells marked as crater rim deposits.
 271 Rim and ejecta locations are tagged when craters are formed, and recorded to the model output
 272 intermittently. We use *DeltaMetrics* to convert timeseries model outputs to a gridded stratigraphic
 273 volume with 10 cm vertical resolution. *DeltaMetrics* determines the time when a given grid elevation
 274 was last occupied by the sediment surface at that location (Schumer et al., 2011), and assigns each
 275 voxel within the stratigraphic volume to reflect the appropriate simulation conditions. This approach
 276 creates a temporal discretization bias, that is minimized by saving model states at a high temporal
 277 resolution with respect to landscape evolution (e.g., Moodie et al., 2021; Moodie & Passalacqua,
 278 2021; Hariharan et al., 2023).

279 Simulations do not include any additional surface processes that would eliminate crater de-
 280 posits or obfuscate crater rims and reduce mappability, including for example, diffusive rim degrada-
 281 tion by wind, water, or subsequent impactors (Öpik, 1966; Hartmann, 1966; Ross, 1968; Soderblom,
 282 1970; Hartmann, 1971; Schultz & Gault, 1975; Hartmann & Neukum, 2001; A. Howard, 2004;
 283 Richardson et al., 2004, 2005; M. R. Smith et al., 2008; Richardson, 2009; Minton et al., 2015).
 284 However, our model implicitly includes crater obliteration by direct overprinting from subsequent
 285 craters (Woronow, 1977, 1978; Minton et al., 2015); we quantified this effect and determined there
 286 to be little affect on our results (Supplementary Material).

287 We ran nine replicate simulations for each of 1 Myr, 10 Myr, and 100 Myr (27 simulations
 288 total) to assess uncertainty and develop a large number of craters for analyses (180,844 craters).
 289 Model replicates for a given delta formation timescale (e.g., all 100 Myr replicates) used different
 290 crater-size distributions synthesized by Monte Carlo simulation.

291 3 Results

292 3.1 Crater rims and ejecta preserved in stratigraphy

293 Landscape development over time (Figure 3) generates stratigraphy that includes fluvial de-
 294 posits and crater rim and ejecta material (Figure 4). From 180,844 craters across all formation du-
 295 ration and replicate simulations, we identified 26,709 interbedded craters. Iterating over each crater,
 296 we identified the initial crater deposit annulus area (i.e., excluding the crater floor), separated the
 297 rim and ejecta material, and calculated 1) the remaining fraction of rim annulus area, 2) the remain-
 298 ing fraction of ejecta annulus area, and 3) the angle subtended by the largest contiguous segment
 299 of the rim annulus remaining (e.g., Figure 4c). For calculation of the remaining rim fraction for a
 300 single crater, for example, we divide the number of model grid cells that include rim material from
 301 that crater at any height in the stratigraphic column, by the number of grid cells that were initially
 302 marked as containing crater rim material for that crater; the remaining ejecta fraction is calculated
 303 in the same manner. Calculation of the preserved rim continuity similarly identifies grid cells with
 304 stratigraphic columns including rim material of that crater, and bins these cells into azimuthal ranges

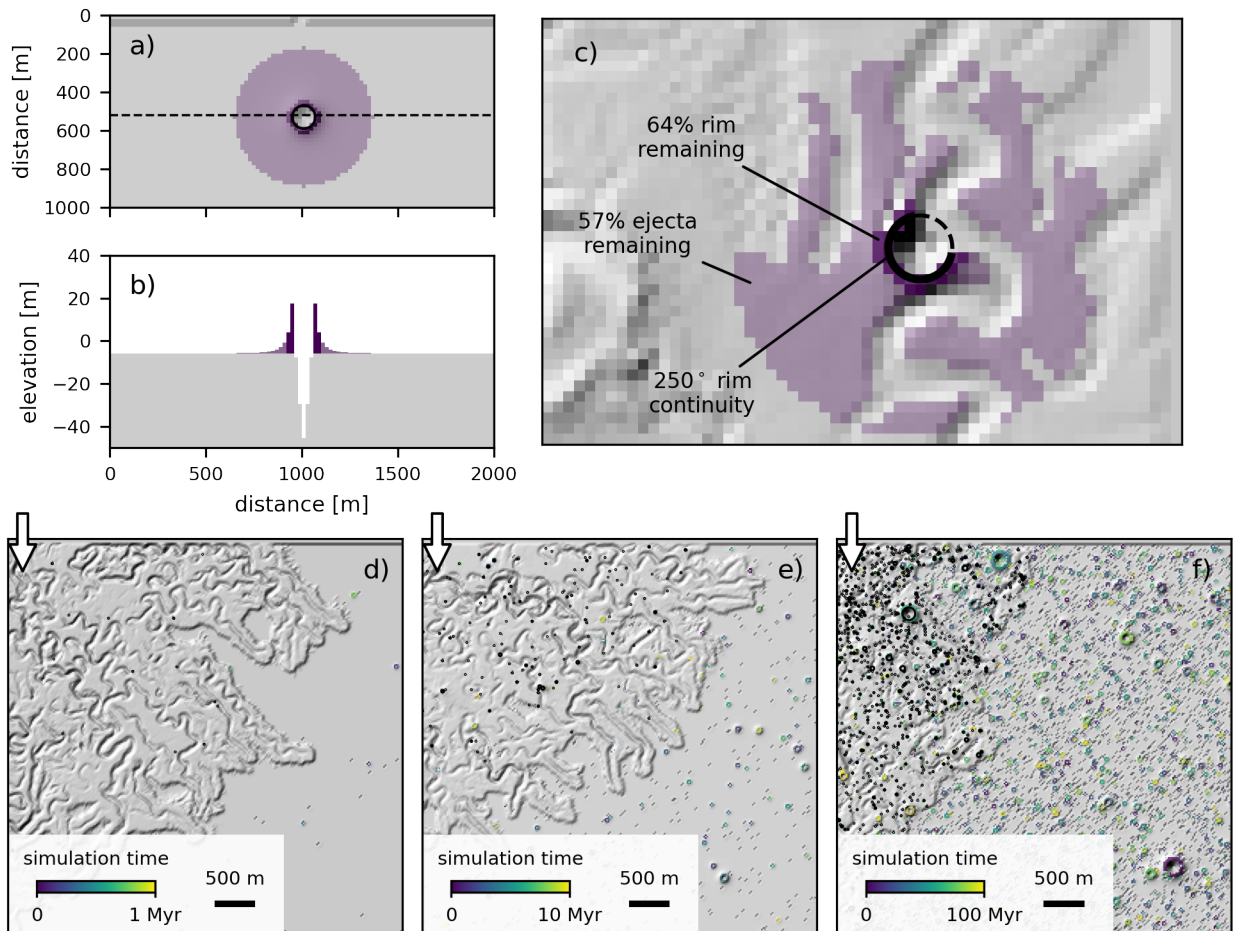


Figure 4. Example of a single pristine crater in a) mapview and b) cross-section, showing the extent of deposits tagged as crater rim (dark purple) and crater ejecta (light purple). c) Example of crater rim and ejecta degraded by fluvial reworking, and study metrics evaluated for this degraded crater. Topographic hillshade of a d) 1 Ma, e) 10 Ma, and f) 100 Ma simulation. Crater rim material *at the deposit surface* is colored by crater formation time, with black circles highlighting interbedded crater rims. The area of each panel is $\sim 27 \text{ km}^2$ (approximately half of the model domain, with white arrows indicating the channel inlet location).

305 with respect to the crater center, and determines the arc length of the largest sector of consecutive
 306 bins. Identifying crater rim and ejecta material anywhere in the stratigraphic volume, rather than
 307 only exposed at the surface, isolates metrics from the effects of exhumational bias (Warren et al.,
 308 2019).

309 All metrics are impacted by model grid discretization effects, but these effects are most ap-
 310 parent for smaller craters, and for the rim fraction and rim continuity metrics. This sensitivity arises
 311 because smaller crater rims occupy only eight grid cells immediately surrounding a single crater-
 312 floor grid cell, which creates, for example, just nine possible quanta for the preserved rim fraction
 313 (0, 0.125, ..., 0.875, 1.0; Figure 5a); in some rare circumstances, time discretization effects intro-
 314 duce additional possible quanta (Supplementary Material).

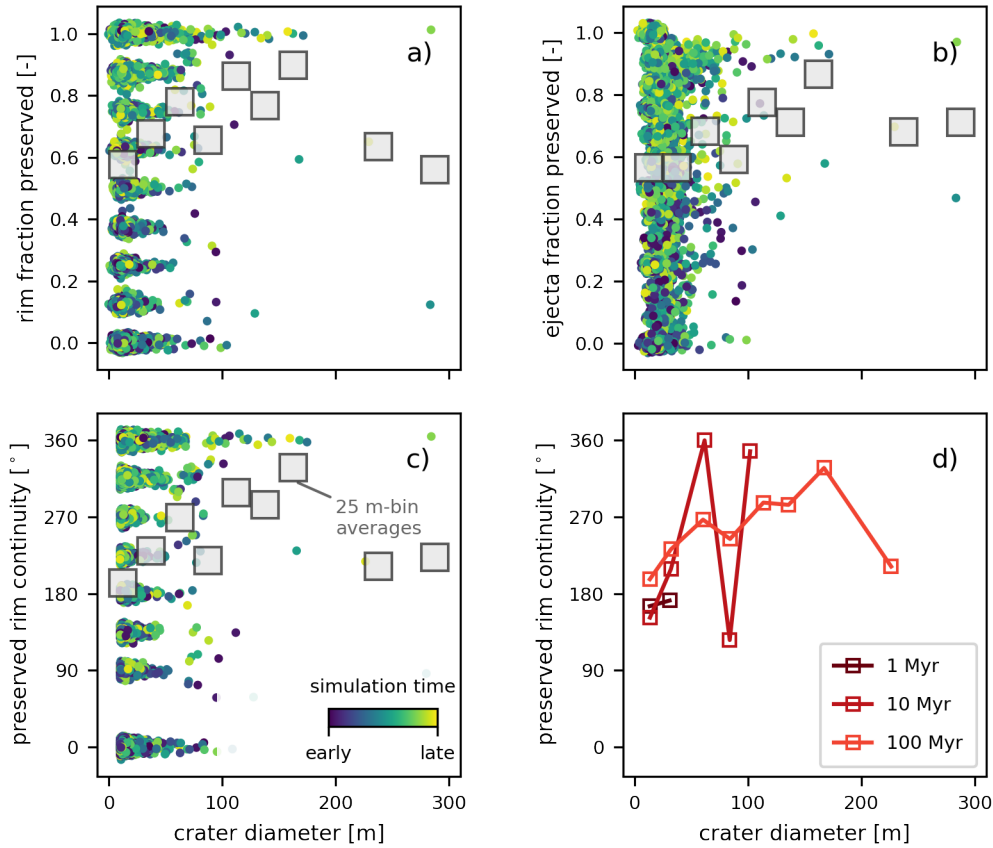


Figure 5. Interbedded crater a) rim fraction preserved, b) ejecta fraction preserved, and c) preserved rim continuity as a function of crater diameter, and colored by crater formation time within a simulation. Data are aggregated across all simulation timescales and replicates, and have normally-distributed noise added to both axes for visualization (mean of 0, and standard deviation of ± 0.01 or $\pm 1.5^\circ$, and ± 1.5 m). Gray boxes mark non-overlapping 25 m-bin averages. d) 25 m-bin averages of preserved rim continuity separated by simulation duration. Total number of craters accumulated (i.e., simulation duration) does not impact the fluvial reworking bias.

315 For crater diameters from 10 to ~ 50 m, the fraction of crater rim and ejecta area preserved
 316 varies between 0.0 and 1.0 (i.e., fully eroded to fully preserved), and this variability decreases as
 317 crater diameter increases, generally converging towards full preservation (Figure 5a,b). Preserved
 318 rim continuity is similarly variable for smaller crater diameters ($\lesssim 50$ m), and converges towards
 319 360° continuity with increasing crater diameter (Figure 5c). Importantly, robust trends in preserva-
 320 tion for larger diameter craters in the size range of interest (150–300 m) are obscured by the fact
 321 that simulations included only seven craters larger than 150 m, due to the nature of crater production
 322 functions (e.g., Figure 2; Ivanov, 2001).

323 Non-overlapping 25 m crater diameter bin averages (gray boxes, Figure 5a–c) show a broad
 324 increase in preservation with increasing crater diameter. Approximately 67% of smaller interbedded-
 325 crater rims ($\lesssim 50$ m) have been at least partially eroded (measured as rim continuity $< 360^\circ$), with
 326 38% having less than half of the rim area remaining, and 44% having less than 180° of preserved
 327 rim continuity. Interestingly, about 53% of larger interbedded-crater rims (crater diameter > 50 m)
 328 were also partially eroded (measured as rim continuity $< 360^\circ$), with 19% and 24% having less than

329 half rim fraction preserved and preserved rim continuity, respectively. Overall, simulations indicate
 330 that fluvial reworking can remove a substantial fraction of interbedded crater deposits, especially
 331 removing smaller crater deposits from the record.

332 Preservation does not depend on the crater accumulation time duration (Figure 5d), or on crater
 333 formation time (Figure 5a–c). When preserved rim continuity data are separated into simulations
 334 representing 1, 10, and 100 Ma and summarized as 25 m-bin averages (Figure 5d), the trend of
 335 each simulation duration set is not distinguishable from the others. Most importantly, for smaller
 336 diameter craters ($\lesssim 50$ m) where data density sufficiently characterizes fluvial reworking bias, there
 337 is little difference in rim continuity for different simulation durations (Figure 5d).

338 **3.2 Biased crater size-frequency cumulative distributions**

339 We made synthetic fluvial reworking-biased crater diameter distributions by Monte Carlo sam-
 340 pling from the simulated crater record, and compare biased distributions to the full interbedded crater
 341 distribution, and to the observed Mars interbedded crater distribution (e.g. Kite et al., 2014). To
 342 generate a CSFD biased by fluvial reworking, we randomly selected 56 craters from the simulated
 343 interbedded crater record (56 is the number of craters observed in the Kite et al. (2014) dataset), and
 344 excluded those craters with $< 180^\circ$ rim continuity. We repeated this process 100 times to assess dis-
 345 tribution variability, and show the median distribution, and 16th to 84th percentile distributions in cu-
 346 mulative probability space, as a solid line and shaded envelope, respectively (Figure 6). Cumulative
 347 distributions are useful to visually highlight (dis)similarity of two distributions as (non)overlapping
 348 lines when plotted (Figure 6); differences in either distribution support (left-to-right shifts) or den-
 349 sity (curve and slope change) create perceptual dissimilarity. We note that a $< 180^\circ$ rim continuity
 350 threshold was also used by Kite et al. (2014) to map craters on Mars, but Warren et al. (2019) ex-
 351 cluded craters with $< 150^\circ$ of topographically elevated rim (including discontinuous sections); we
 352 thresholded based on continuous rim arc length because it is considerably simpler to implement for
 353 automatic calculation. Sensitivity testing revealed that differences in the threshold (120° – 240°) and
 354 the number of craters (40–72) do not impact results.

355 The cumulative distributions biased by fluvial reworking are similar to the cumulative distribu-
 356 tion of all interbedded craters (Figure 6). Additionally, there is little variability among the sampled
 357 fluvial reworking-biased distributions (i.e., between the 16th and 84th percentile distributions; Fig-
 358 ure 6). The sampled fluvial reworking-biased distributions have a distinct range and density from
 359 the Kite et al. (2014) observed crater diameter distribution (Figure 6). For example, the fluvial
 360 reworking-biased distributions are dominated by crater diameters 10–20 m approximately following
 361 an exponential distribution, whereas the observed data approximately follows a one-sided truncated
 362 normal distribution with the smallest observed diameter ~ 35 m (Figure 6).

363 In addition to fluvial reworking, measured interbedded crater-size distributions are biased by
 364 exhumational processes that preferentially expose larger craters buried within stratigraphy (Kite
 365 et al., 2013). Preferential exhumation is due to geometric constraint that a quasi-horizontal plane
 366 cutting through a rock volume will sample features from the volume proportional to the features’
 367 length scale along the axis normal to the quasi-horizontal plane (Russ, 1986; Yielding et al., 1996).
 368 Assuming semi-hemispherical craters with a fixed ratio between crater diameter and depth (e.g.,
 369 Melosh, 1989), the proportion of craters sampled on a quasi-horizontal plane is therefore dependent
 370 on crater depth (i.e., the vertical crater length; Lewis & Aharonson, 2014), or following the fixed
 371 depth-diameter ratio, crater exhumation bias is proportional to crater diameter (Kite et al., 2014).
 372 Our study examines crater rim and ejecta deposits, and we similarly assume a fixed ratio between
 373 crater depth and rim height, such that exhumation bias is linearly proportional to crater diameter.

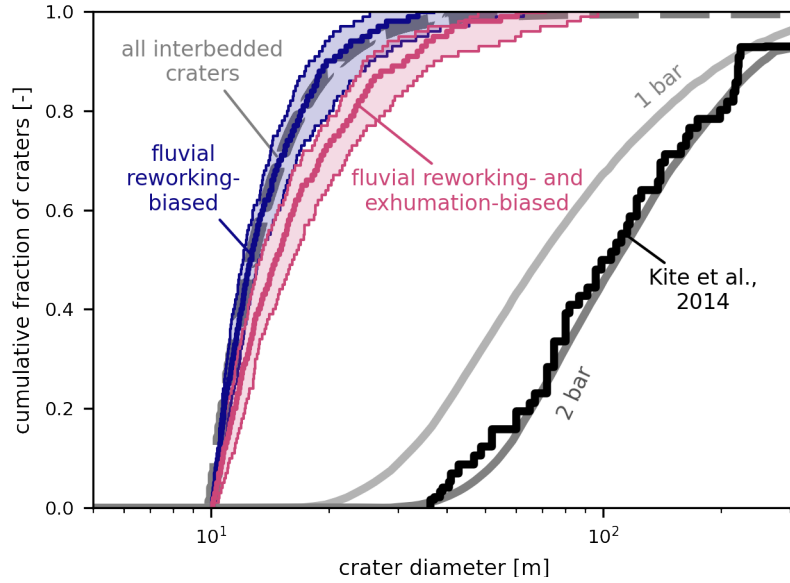


Figure 6. Empirical crater size distributions of all modeled interbedded craters (dashed gray line), preserved and mappable craters after applying fluvial reworking bias (blue) and fluvial plus exhumation biases (pink), and interbedded craters mapped by Kite et al. (2014) (solid black line); results are compared to crater size distributions predicted for paleo-atmospheric pressures (solid gray lines) from (Kite et al., 2014). For preserved and mappable crater size distributions, the biases applied are fluvial reworking (blue), and fluvial plus exhumational bias (pink). Calculated distributions are shown by the median (solid line), and envelope from the 16th to 84th percentile distributions (shaded area).

374 Note, the crater depth/height-to-diameter ratio is not explicitly included in the proportionality, so
 375 the relevant assumption is just that this ratio is fixed over the size range of interest.

376 We model exhumation bias by applying an increased weighting to larger craters in Monte
 377 Carlo sampling to generate synthetic crater diameter distributions from simulations. Probability
 378 for a crater with diameter d to be included in the synthetic distribution goes as $p(d) \propto d/d_{min}$,
 379 where $d_{min} \approx 10$ m is the smallest crater diameter in the simulations. We empirically tested whether
 380 exhumational bias follows this proportionality, and determined that it is a reasonable first-order
 381 approximation of the bias imparted by exhumation, but that bias depends on the relative rate of
 382 deposit accumulation and crater production, and assumptions of crater geometry (Section 4.4.3;
 383 Supplementary Materials).

384 Cumulative distributions biased by fluvial reworking and exhumation have a marked increase
 385 in larger craters, with respect to the distribution of all interbedded craters (Figure 6). Still, the
 386 distributions are dominated by 10–30 m diameter craters, and remain substantially different in shape
 387 and scale from the observed crater-size distribution (Figure 6).

388 4 Discussion

389 4.1 Fluvial reworking bias does not explain observed crater populations

390 Despite nearly half of smaller craters ($\lesssim 50$ m) having $<180^\circ$ remaining rim continuity and
 391 potentially not being mappable, the shift in the cumulative CSFD due to fluvial reworking is very

392 small (Figure 6). This small shift arises because the CSFD is dominated by smaller craters: there
393 are ~ 340 times more interbedded and mappable ($>180^\circ$ rim continuity) craters sized 5–15 m than
394 sized 55–65 m (18,743 and 55 craters, respectively). The relative abundance of smaller craters
395 is a factor of the crater production function, and although the true crater production function is
396 unknown, the approximately exponential form of the function is not disputed (Fassett, 2016). So,
397 although fluvial reworking can remove many smaller craters, the dominance of smaller craters in
398 the CSFD is inescapable, and fluvial reworking cannot bias the crater record to the extent needed
399 to explain observed distributions. Notably, even in the extreme case of a delta formed over 1 Myr,
400 which leads to the smallest number of accumulated craters (Figure 2), fluvial reworking does not
401 modify the CSFD enough to match observations on Mars (Figure 5d; Supplementary Material).

402 Our findings are consistent with previous studies that hypothesize fluvial reworking is not
403 a primary control on observable crater size-frequency distributions of ancient interbedded craters
404 on Mars (Kite et al., 2014; Warren et al., 2019). Our results indicate that fluvial reworking is a
405 subordinate control because of the overwhelming number of smaller craters generated, rather than
406 the notion that crater deposits are not eliminated from the stratigraphic record (indeed, many crater
407 deposits are eliminated by fluvial reworking; e.g., Figures 3 and 5). Though lateral migration and
408 avulsion place channels across the entire delta over time, channels occupy only a small fraction
409 of the delta surface at any moment in time (Reitz & Jerolmack, 2012), such that the majority of
410 new interbedded craters are formed away from active channels. Interestingly, a crater must be at
411 least partially buried by fluvial sediments to be considered an interbedded crater for this study, so it
412 appears that craters formed away from active channels receive distally deposited fine sediment, but
413 that many crater locations must not be revisited by a channel during the simulation. In summary,
414 our simulations show that fluvial reworking, by way of lateral migration and avulsion, is not able to
415 remove smaller craters at the pace they are created.

416 Our conclusions bolster studies that use the lack of smaller interbedded craters as evidence
417 for a higher pressure ancient atmosphere. In contrast to migrating rivers that intermittently visit
418 locations on the landscape, a planetary atmosphere exists everywhere above the landscape and is in
419 place to brake and ablate all incoming impactors. For example, in the case of an atmosphere with
420 stable pressure, there is a lower limit to the diameter of impactors that survive atmospheric ablation,
421 translating to a lower limit on crater diameters formed (Kite et al., 2014). Though paleo-pressure
422 may have fluctuated in the past (Warren et al., 2019), we see very little possibility for atmospheric
423 pressure to have remained low enough for long enough that a substantial number of smaller craters
424 would have formed *and* subsequently be eliminated by fluvial reworking. Instead, a more likely
425 scenario is that the smaller craters never formed, due to higher atmospheric pressure. Moreover,
426 the sustained and intense fluvial activity that would be needed to rework enough smaller craters to
427 reproduce observed distributions would be highly unlikely without at least some atmosphere (e.g.,
428 Kite, 2019; Kite et al., 2022), which would therefore inhibit formation of smaller craters in the first
429 place. In summary, simulation results indicate that although rivers are sometimes in the right place
430 to remove smaller craters, an atmosphere is always in place to remove small impactors and prevent
431 formation of smaller craters altogether.

432 **4.2 The functional form of the fluvial reworking filter**

433 Although fluvial reworking cannot account for the lack of smaller interbedded craters observed
434 on Mars, our modeling results indicate that fluvial erosion can remove a significant proportion of
435 these craters from the stratigraphic record. Creating a well-calibrated crater removal function could
436 bolster atmospheric paleo-pressure interpretations. Moreover, a set of calibrated crater removal

437 functions could be used to infer characteristics of ancient river migration and avulsion, for example,
 438 from divergences between observed CSFDs and those predicted for atmospheric filtering from an
 439 independently constrained paleo-pressure. It would be problematic to calibrate a crater removal
 440 function from our simulation results heretofore, because simulations include a limited number of
 441 larger interbedded crater observations (only seven craters $\gtrsim 150\text{--}300$ m; Figure 5). The limited
 442 number of larger craters is a realistic constraint, imposed by the nature of crater production in the
 443 solar system (e.g., Figure 2b,c; Ivanov, 2001), but relaxing this constraint could refine our view of
 444 crater reworking over the complete range of crater sizes of interest (10–300 m).

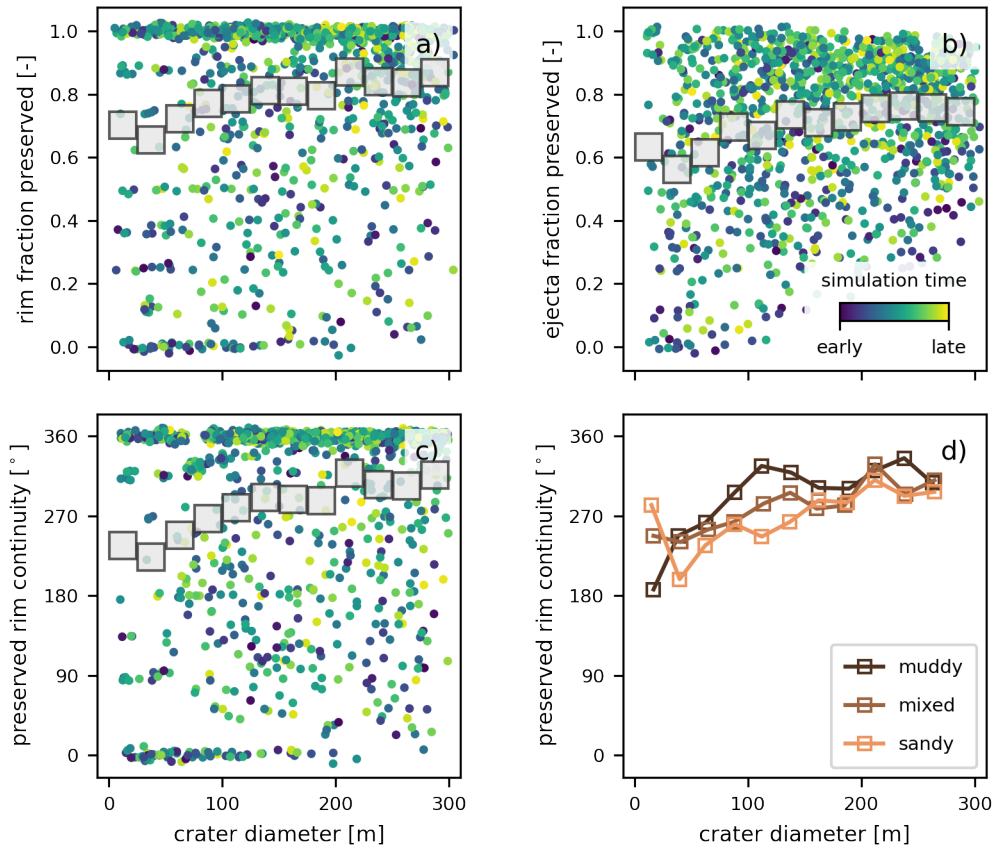


Figure 7. Interbedded crater a) rim fraction preserved, b) ejecta fraction preserved, and c) preserved rim continuity as a function of crater diameter for uniform crater size-frequency distribution. Data are aggregated across all input sediment compositions and replicates, and up to ± 0.1 or $\pm 1.5^\circ$ and ± 1.5 m point jitter is added for visualization. Gray boxes mark mutually exclusive 25 m-bin averages. Calculated metrics show that preservation is varied, but on average increases with increasing crater diameter. d) 25 m-bin averages of preserved rim continuity separated by sediment composition input to the delta. Increasing input sandiness led to a decrease in preserved rim continuity, i.e., an increase in fluvial reworking bias.

4.2.1 Uniform crater size-frequency distribution simulations

446 To increase observations of interbedded craters $\gtrsim 150$ m in diameter, We ran additional simu-
 447 lations with a uniform crater size-frequency distribution (i.e., craters of all diameters 10–300 m are
 448 equally likely). Simulation parameters otherwise remained the same as previous simulations, except

449 for two modifications. First, we limited the number of craters per simulation to 250 and increased the
 450 number of replicate simulations, because too many larger craters in a single simulation introduced
 451 numerical instability to the delta model. Second, we varied sediment composition input to the delta
 452 (Liang et al., 2016; Moodie & Passalacqua, 2021), to assess how channel mobility modulates the
 453 fluvial reworking filter. We varied the input sediment mixture from a muddy to sandy composition
 454 (sand fraction 0.2, 0.5, and 0.8) across 36 runs (12 replicates for each sand fraction), yielding 9000
 455 craters and 1180 interbedded craters to examine preservation metrics (Figure 7).

456 We computed the rim fraction preserved, ejecta fraction preserved, and rim continuity in the
 457 same manner as previous simulations (Figure 7a–c). Similar to size–frequency distribution simula-
 458 tions, uniform size distribution simulations indicate varied preservation, ranging from undegraded
 459 craters to complete removal. 25 m-bin averages indicate that preservation generally increases with
 460 crater size (Figure 7a–c). Notably, uniform size distribution simulations characterize average fluvial
 461 reworking bias more smoothly and over a more complete crater diameter range than size-frequency
 462 distribution simulations (Figures 5 and 7).

463 Splitting simulations by input sediment composition reveals differences in average preserva-
 464 tion of smaller crater deposits (Figure 7d). Muddy simulations resulted in higher preservation than
 465 sandy simulations on average (Figure 7d). Average preservation in muddy simulations shows a non-
 466 linear dependence on crater diameter (with preservation dropping steeply below $\lesssim 100$ m), whereas
 467 sandy simulations have an approximately linear dependence on crater size (Figure 7d). As de-
 468 scribed in Section 2.2, DeltaRCM simulations of sandy deltas have higher rates of channel mobility
 469 and therefore increased sediment reworking relative to muddy deltas (Liang et al., 2015a; Hariha-
 470 ran et al., 2021). Differences in fluvial reworking for different sediment compositions are second
 471 order to the size-dependent trend, and are consistent with a process-based understanding of channel
 472 dynamics and stratigraphic preservation (Hajek & Straub, 2017; Hariharan et al., 2021).

473 **4.2.2 Calibrating crater removal by the fluvial reworking filter**

We define a filtering function, representing the bias applied to the interbedded crater record by
 fluvial reworking:

$$c = 1 - \exp\left(-\frac{(d_0 - d)}{n}\right), \quad (1)$$

474 where c is the fraction of craters of size d remaining, d_0 is a reference crater diameter, and n is the
 475 “e-folding” crater diameter at which 60% of craters with $d = d_0 + n$ are preserved (Warren et al.,
 476 2019). The functional form of the filter is after the Warren et al. (2019) crater removal factor, and
 477 is redefined as a continuous function, with conditions that Equation 1 is valid only for d in $[0, \infty)$
 478 and values of c are bounded in $[0, 1]$ (i.e., $c = \max(0, c)$). Figure 8 shows Equation 1 determined
 479 with parameters from Warren et al. (2019) for Meridiani ($d_0 = 15.7, n = 23$), and for parameters
 480 determined from Bayesian estimation for our simulation results. For model parameter estimation, we
 481 assume normally distributed priors, and determine mappable fraction from the 25 m-bin averages of
 482 rim continuity from the uniform crater size-frequency distribution simulations thresholded at 180° ,
 483 treating the muddy and sandy simulations separately (i.e., data are after Figure 7d). We defined
 484 the mappable crater fraction using the rim continuity data because this metric is commonly used
 485 as a threshold criteria in crater counting (Kite et al., 2014; Warren et al., 2019), and other metrics
 486 would be difficult to constrain outside of the model. For the muddy simulations, the estimated
 487 model parameters are $d_0 = -48 \pm 8$ and $n = 78 \pm 7$, and for the sandy simulations, estimated model
 488 parameters are $d_0 = -286 \pm 9$ and $n = 288 \pm 9$. We note that reference diameters $d_0 < 0$ have no
 489 physical meaning, and occur due to removing the constraint of full reworking (i.e., zero potentially

490 mappable craters) at a crater diameter >0 (e.g., Warren et al., 2019); this constraint is not supported
 491 by any empirical evidence or theory (Figure 7).

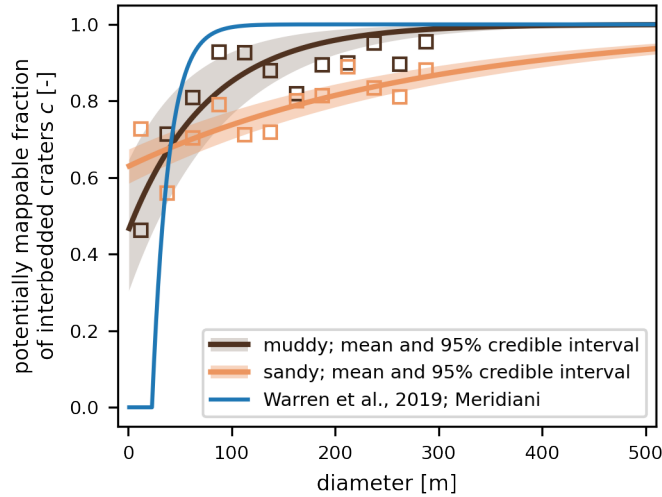


Figure 8. Potentially mappable fraction of interbedded craters as a function of crater diameter. The blue curve is Equation 1 with parameters from Warren et al. (2019) for Meridiani ($d_0 = 15.7, n = 23$). The brown and orange curves and shaded areas are Equation 1 evaluated with estimated model parameters and 95% credible intervals for muddy and sandy simulations, respectively. Data for parameter estimates are derived from a 180° rim continuity threshold, and therefore includes buried craters (i.e., excludes exhumation bias).

492 The filter proposed by Warren et al. (2019) captures the nature of the relationship between flu-
 493 vial reworking and average crater preservation, but their parameterization underestimates the range
 494 over which reworking occurs, and overestimates the degree to which reworking changes with crater
 495 diameter (Figure 8). Our calibrated models have a larger e-folding crater diameter (n), and because
 496 we do not constrain $d_0 > 0$, our parameterizations maintain a proportion of potentially mappable
 497 craters ($c > 0$) at even the smallest crater diameters. Differences in crater preservation patterns
 498 between the muddy and sandy simulations lead to distinct estimated parameters for these sedimen-
 499 tological systems (Figure 8), though difference due to sediment input is small with respect to the
 500 difference from the Warren et al. (2019) parameterization. Estimated values of n characterize the
 501 sensitivity of reworking to change in crater diameter in Equation 1, with smaller values of n repre-
 502 senting increased sensitivity in muddy simulations.

503 **4.2.3 Implications and potential applications of the crater removal function**

504 Fluvial reworking bias can be accounted for where a sufficient density of craters is present, and
 505 Equation 1 can therefore bolster atmospheric paleo-pressure interpretations. For example, Equation
 506 1 can integrate into an inference framework that improves atmospheric paleo-pressure estimates, by
 507 considering the observed CSFD as it is found, after being biased by atmospheric filtering and flu-
 508 vial reworking (in that order). This framework would shift interpreted paleo-pressure upper-bounds
 509 (e.g., Kite et al., 2014; Warren et al., 2019) to now-lower paleo-pressure estimates with meaningful
 510 uncertainty; for example, CSFDs modeled for different atmospheric pressures and fluvial reworking
 511 would steepen and rotate counter-clockwise, becoming increasingly convex-up at smaller diameters.

512 We emphasize that our estimated fluvial reworking filter characterizes the fraction of craters pre-
 513 served on average (with a measure of variability), and so any revised paleo-pressure interpretations
 514 using this filter should carry uncertainty due to variability (Figure 8). Additionally, our estimated
 515 fluvial reworking filter implicitly incorporates the effects of crater obliteration during formation of
 516 new craters, and so may slightly overestimate the effect of fluvial reworking bias alone (Supplemen-
 517 tary Materials); we cannot separate crater obliteration from fluvial reworking in our simulations, as
 518 is the case in natural systems. To be complete, an inversion framework should incorporate additional
 519 crater-degrading surface processes and possible sources of bias (exhumation bias has already been
 520 incorporated in these frameworks; Kite et al., 2014); but importantly, we do not expect these factors
 521 to significantly impact crater counts (Section 4.4).

522 Details of sediment composition and channel characteristics that prevailed on ancient Mars
 523 are not well constrained (J. P. Grotzinger et al., 2015; Stack-Morgan et al., 2023), so model-fit pa-
 524 rameterizations should be interpreted as scenarios that estimate a plausible range of reworking bias.
 525 Interestingly, it may be possible to infer ancient channel dynamics from mapped CSFDs if atmo-
 526 spheric paleo-pressure is independently constrained. For example, the crater-diameter range over
 527 which the observed crater size-frequency distribution deviates from the known paleo-pressure ex-
 528 pected distribution, could inform whether ancient channel dynamics were more similar to dynamics
 529 of channels in muddy or sandy simulations.

530 **4.3 Crater removal determined by channel avulsion frequency and channel geometry**

531 We interpret the difference in average preservation between muddy and sandy simulations to
 532 be due to varied channel mobility modes and varied channel geometry between the cases, which
 533 are well known to be modulated by the sand fraction input to DeltaRCM (Section 2.2; Liang et al.,
 534 2015a, 2016; Moodie & Passalacqua, 2021). To briefly summarize simulation differences, muddy
 535 simulations exhibit narrower and deeper channels that remain in place longer before delta-scale
 536 avulsions relocate channels, whereas sandy simulations maintain shallower and wider channels that
 537 frequently avulse at multiple scales. These model behaviors are consistent with a process-based
 538 understanding of controls on channel geometry (Dunne & Jerolmack, 2018; Dong et al., 2019;
 539 Dunne & Jerolmack, 2020) and avulsion (Mohrig et al., 2000; Slingerland & Smith, 2004; Straub et
 540 al., 2015).

541 We originally hypothesized that larger craters (~ 50 – 300 m diameter) have rims rising above
 542 the delta plain that would present a physical obstacle to flow, and therefore not be reworked and
 543 removed from the stratigraphic record. Our results repeatedly document a crater diameter-dependent
 544 bias (e.g., Figures 5 and 7), and here we interpret observed crater preservation patterns in the context
 545 of hypothesized topographic steering. It is important to emphasize that differences between muddy
 546 and sandy preservation are only apparent in *average* behavior (Figure 7d, Figure 8), and that both
 547 cases exhibit varied preservation ranging from craters that are fully eliminated to fully preserved.

548 Channel avulsions cause flow to spread across the delta landscape, generally following topo-
 549 graphic gradients to a new outlet on the coast (Jerolmack & Paola, 2007; Reitz et al., 2010). In
 550 our simulations, flow during avulsion is steered by self-organized delta topography and by crater
 551 topography; an example of flow steered by self-organized topography during an avulsion is shown
 552 in Figure 3f–g. Infrequent avulsions in muddy simulations create significant self-organized topo-
 553 graphic roughness (e.g., Liang et al., 2016), such that if flow encounters crater topography during
 554 an avulsion, it may be steered towards a nearby topographic low, wherein a new channel is formed
 555 (e.g., Figure 3f–g). Frequent avulsions in sandy simulations distribute sediment more evenly across
 556 the deltaic landscape, such that topographic lows are rapidly filled and topographic variability is

557 relatively small (e.g., Liang et al., 2016). Therefore, when an avulsion occurs in sandy simulations,
 558 flow is not easily steered by crater topography towards a topographic low (i.e., because there are no
 559 significant topographic lows). The effect of these differences, on average, is that the overall crater
 560 removal fraction is higher in sandy simulations (Figure 8), and crater removal is less sensitive to
 561 crater size in sandy simulations (Figure 8). Said another way, the presence of topographic lows in
 562 muddy simulations enhances the size-dependent bias that removes smaller craters from the crater
 563 record, but reduces reworking overall.

564 From a geometric perspective, fluvial reworking occurs where a channel cross-section inter-
 565 sects with deposited sediments, and so is limited to the landscape area visited by channels, and
 566 extends into the subsurface up to the channel depth. This perspective implies that more frequent
 567 avulsions would increase fluvial reworking, and also that deeper channels would increase fluvial
 568 reworking. Sandy simulations, which have shallower channels and more frequent avulsions than
 569 muddy simulations, exhibit higher average reworking. This indicates that crater deposit reworking
 570 is more sensitive to avulsion frequency than channel depth. We expect that processes influencing
 571 crater removal in uniform crater size-frequency distribution simulations also modulate reworking
 572 in our primary simulations with CSFDs synthesized from a production function. Reworking in pri-
 573 mary simulations is likely transitional between reworking observed in muddy and sandy simulations,
 574 because the input sand fraction in these cases is the same.

575 There are some additional factors of the model design and simulation configurations that could
 576 affect reworking. Reworking could increase in a situation where a river or delta is confined by
 577 valley walls, because a higher proportion of the active fluvial area (i.e., floodplain) is occupied by
 578 channel area (Dong & Goudge, 2022). By similar logic, braided rivers that occupy a larger fractional
 579 area of the active fluvial area (Tejedor et al., 2022; Dong & Goudge, 2022) could show a higher
 580 proportion of crater reworking. Thus, we would the number of intersections between interbedded
 581 craters and channel cross sections to increase, thereby enhancing crater removal. Additionally, river
 582 bend migration in confined valleys can be dominated by down-valley bend translation that eliminates
 583 strata over the full valley width (Limaye & Lamb, 2013). However, it is not currently known whether
 584 Aeolis Dorsa, or other paleo-channel features were formed in confined valleys or on broad alluvial
 585 plains (Cardenas et al., 2017; Dong & Goudge, 2022).

586 **4.4 Degradation, obliteration, exhumation, and image resolution as potential sources of** 587 **bias**

588 Crater degradation is the erosion of crater rims and infilling of crater floors by sedimentary
 589 processes, so that crater topographic expression is gradually diminished over time (Craddock et
 590 al., 1997; Forsberg-Taylor et al., 2004; M. P. Golombek et al., 2014). We did not include any
 591 crater degradation effects in our model, so a natural question is whether including these processes,
 592 in conjunction with fluvial reworking bias, could meaningfully impact the observable smaller crater
 593 record on Mars. In this section, we examine several processes and effects that alter crater topography
 594 on ancient and modern Mars. We comment on whether these processes could impact modeling
 595 results, and speculate on how sensitive counting of interbedded craters on Mars is to these processes.

596 **4.4.1 Wind and aeolian erosion**

597 M. P. Golombek et al. (2014) found that aeolian erosion degrades recently formed smaller
 598 crater rims on modern Mars at up to 1 m/Myr, but that this rate quickly declines to 0.1 m/Myr;
 599 longer-term rates are as low as 0.001 m/Myr (M. P. Golombek et al., 2006). Aeolian sedimentation
 600 rates during the period of fluvial activity of interest beginning 3.5 Ga are poorly constrained, but

601 modern rates of erosion serve as a helpful proxy for the following thought experiment. For a crater
602 rim height to diameter ratio of ~ 0.04 (Pike, 1977; Melosh, 1989; Robbins & Hynes, 2012), we
603 expect freshly formed crater rims < 1 m high for craters smaller than 30 m. This rim height is
604 sufficiently small that wind-blown degradation rates up to 1 m/Myr could substantially weather
605 craters before entering the stratigraphic record.

606 Our simulations spanned a range of plausible delta formation timescales 1, 10, and 100 My
607 (Bhattacharya, 2005; Buhler et al., 2014; Irwin et al., 2015; Lapôtre & Ielpi, 2020). In the ex-
608 treme case of a delta forming intermittently over 100 My and aeolian erosion occurring at similar
609 rates to modern craters, a crater formed on the delta surface would be weathered for several million
610 years before a channel returns to the area to potentially bury the crater deposit (Figure 3). In such a
611 situation, it is possible that smallest-crater rims could be substantially degraded before being incor-
612 porated into the stratigraphic record, and therefore be unrecognizable as craters after exhumation. At
613 more moderate timescales of delta formation and lower crater degradation rates, we do not anticipate
614 that crater rims would be substantially degraded before potential incorporation into the stratigraphic
615 record. Future modeling could consider how craters of varying degrees of degradation are incorpo-
616 rated into the stratigraphic record and later exhumed as landforms observable on the modern Mars
617 surface (e.g., Cardenas et al., 2022). Importantly, even if wind degrades all or a significant fraction
618 of craters below 30 m before burial, our conclusions would not change, because mappable cumula-
619 tive crater-size distribution shape would likely still be dissimilar to Mars observations (e.g., Figure
620 6).

621 **4.4.2 Crater obliteration**

622 Obliteration of an existing crater rim or ejecta deposit by the formation of a new impact crater
623 leads to a steady state crater size-frequency distribution, which deviates at smaller crater diameters
624 from the distribution dictated by the crater production function (Woronow, 1977, 1978; M. R. Smith
625 et al., 2008; Richardson, 2009; Minton et al., 2015). This crater obliteration processes is implic-
626 itly included in our simulations, though our simulations accumulate far fewer craters than needed
627 to approach a steady state distribution. Nevertheless, we ran nine simulations without river-delta
628 sediment input, and then generated craters according to 100 Myr of elapsed time beginning 3.5 Ga,
629 and quantified preservation using the same routine as the main text. In these simulations, we find
630 that smaller craters are preferentially rendered unmappable by obliteration (consistent with prior
631 research), but that the magnitude of crater removal by obliteration is far less than fluvial reworking,
632 and therefore does not affect our study interpretations. For example, crater obliteration removes
633 $\sim 10\%$ of crater rim area for craters $\lesssim 50$ m, $\sim 10\%$ of crater ejecta area for all crater sizes mod-
634 eled, and similarly minimally impacts the preserved rim continuity. Importantly, these obliteration
635 metrics represent upper bounds on crater obliteration bias, because craters remain at the modeled
636 surface and there is no mechanism to incorporate crater material into stratigraphy and away from
637 the surface new craters form on.

638 We do not expect that Mars interbedded crater records are significantly affected by crater
639 obliteration during formation of new craters. Interbedded craters would have formed on active sedi-
640 mentary surfaces that would not have persisted long enough for an equilibrium density of craters to
641 form.

642 **4.4.3 Exhumational bias of larger craters**

643 Exhumational bias preferentially exposes larger craters, when a sedimentary volume with in-
644 terbedded craters is eroded (Kite et al., 2013). To represent this process in our analysis, we relied

645 on previous research that presents a geometry-based theory for how this bias impacts crater size-
646 frequency distributions (Lewis & Aharonson, 2014). We attempted to empirically validate this
647 theory in the course of our research, and found that the theory provides an acceptable first-order
648 approximation of the effect. Still, we determined that there is an opportunity for further research to
649 improve our understanding of exhumational bias in crater records (Supplementary Material).

650 In any case, we do not expect that plausibly enhanced exhumational bias would impact our
651 primary conclusion that fluvial reworking cannot reproduce observed Mars crater-size distributions.
652 Our attempts to validate the exhumational bias theory indicate that the level of bias needed to remove
653 enough smaller craters to explain the observed Mars crater record is not plausible. Importantly, an
654 improved understanding of exhumational bias will be necessary to incorporate the fluvial reworking
655 process into inference frameworks (e.g., Section 4.2.3).

656 **4.4.4 Image and data resolution**

657 Crater mappability is affected by horizontal and vertical image resolution, as well as image illu-
658 mination angles (Williams et al., 2018). Craters smaller than $3 \times$ data resolution (dx) are not reliably
659 mapped (Richardson, 2009), which provides a reasonable estimate of the lower bound of potentially
660 mappable craters in any dataset. Crater measurements generated by Kite et al. (2014) used HiRISE
661 images (0.25–0.5 m/pixel) that yield gridded digital terrain models (DTMs) with approximately 2–
662 3 m horizontal resolution, and vertical precision on the order of tens of centimeters (McEwen et
663 al., 2007; Beyer et al., 2018). Freshly-formed crater rim heights are approximately 4% of the crater
664 diameter (Robbins & Hynes, 2012), so craters ≥ 5 m would have rim heights ≥ 20 cm, and can be
665 reasonably expected to be mappable in DTMs derived from HiRISE imagery. Therefore, we do not
666 expect data resolution to impact mappable crater counts in previous Mars studies, but CSFDs gen-
667 erated without high-resolution images are unlikely to generate reliable paleo-atmospheric pressure
668 estimates.

669 As mentioned previously, embedded craters that become exposed at the surface by exhumation
670 could be degraded by aforementioned modern sedimentary processes (i.e., wind-blown erosion).
671 Interestingly, these processes could render craters that are fully preserved in the fluvial reworking
672 sense, to become unmappable at present day, due to post-exhumation erosion that lowers observable
673 rim heights below image resolution thresholds. We cannot rule out that modern erosion of ancient
674 interbedded craters affects mappable crater distributions on Mars (Williams et al., 2018), but also
675 do not expect this effect to invalidate upper-bound paleo-pressure interpretations, because including
676 potentially omitted smaller craters would lower upper-bound estimates.

677 **5 Conclusions**

678 In this study, we perform a quantitative evaluation of the potential for fluvial reworking of
679 sedimentary deposits to impart a size-dependent bias on crater size-frequency distributions. Our
680 modeling approach reveals that as many as 67% of smaller craters ($\lesssim 50$ m diameter) are at least
681 partially eroded, with 38–44% of smaller craters having less than half the initial deposit remain-
682 ing, and that preservation of craters is highly variable. Notably, average crater preservation de-
683 creases with decreasing diameter, confirming the presence of a size-dependent fluvial reworking
684 bias. However, the nature of crater size-frequency distributions (i.e., an approximately exponential
685 increase in crater frequency with decreasing diameter) creates a condition where fluvial reworking
686 cannot remove enough smaller craters to meaningfully bias interbedded crater records. That is to
687 say, although fluvial reworking preferentially removes smaller crater deposits from the stratigraphic

688 record, there are too many smaller craters produced for preserved crater size-frequency distributions
 689 to meaningfully change. This conclusion ultimately bolsters paleo-pressure studies that rely on these
 690 interbedded crater records. We developed a function that predicts average fraction of craters that re-
 691 main mappable in stratigraphy after fluvial reworking bias, and estimated parameters of the function
 692 for a range of plausible channel dynamics. Overall, our findings bolster studies that assert fluvial
 693 reworking is not a primary control on smaller interbedded crater counts on Mars.

694 Open Research Section

695 All data, custom model scripts, and analysis scripts used in this research are archived on the
 696 corresponding author's Github page at https://github.com/amoodie/paper_resources in a folder titled
 697 "Moodie_marscraterreworking". Upon acceptance of this article for publication, the authors will
 698 archive the aforementioned folder, along with complete copies of versioned models and bespoke
 699 software used in this research, in a Zenodo repository (doi 10.5281/zenodo.10050333).

700 Acknowledgments

701 The authors gratefully acknowledge David Mohrig for helpful conversations that guided this re-
 702 search. A.M. was supported by a Jackson School of Geosciences Postdoctoral Fellowship at the
 703 University of Texas at Austin. Enter acknowledgments here. This section is to acknowledge fund-
 704 ing, thank colleagues, enter any secondary affiliations, and so on.

705 References

- 706 Beyer, R. A., Alexandrov, O., & McMichael, S. (2018). The ames stereo pipeline: Nasa's open
 707 source software for deriving and processing terrain data. *Earth and Space Science*, *5*(9),
 708 537–548. doi: 10.1029/2018EA000409
- 709 Bhattacharya, J. P. (2005). Dynamic river channels suggest a long-lived noachian crater lake
 710 on mars. *Geophysical Research Letters*, *32*(10). Retrieved from [https://doi.org/](https://doi.org/10.1029/2005gl022747)
 711 [10.1029/2005gl022747](https://doi.org/10.1029/2005gl022747) doi: 10.1029/2005gl022747
- 712 Bishop, J. L., Fairén, A. G., Michalski, J. R., Gago-Duport, L., Baker, L. L., Velbel, M. A., ...
 713 Rampe, E. B. (2018, February). Surface clay formation during short-term warmer and wetter
 714 conditions on a largely cold ancient mars. *Nature Astronomy*, *2*(3), 206–213. doi: 10.1038/
 715 s41550-017-0377-9
- 716 Braat, L., Brückner, M., Sefton-Nash, E., & Lamb, M. (2023, April). Gravity-driven differences
 717 in fluvial sediment transport fluxes on mars and earth. *none*. Retrieved from [https://](https://doi.org/10.31223/x5bq0r)
 718 doi.org/10.31223/x5bq0r doi: 10.31223/x5bq0r
- 719 Bridge, J. S., & Mackey, S. D. (1992). A theoretical study of fluvial sandstone body dimensions.
 720 In *The geological modelling of hydrocarbon reservoirs and outcrop analogues* (pp. 213–236).
 721 John Wiley & Sons, Ltd. doi: 10.1002/9781444303957.ch14
- 722 Buhler, P. B., Fassett, C. I., Head, J. W., & Lamb, M. P. (2014, October). Timescales of fluvial activ-
 723 ity and intermittency in milna crater, mars. *Icarus*, *241*, 130–147. Retrieved from [https://](https://doi.org/10.1016/j.icarus.2014.06.028)
 724 doi.org/10.1016/j.icarus.2014.06.028 doi: 10.1016/j.icarus.2014.06.028
- 725 Cabrol, N. A., Grin, E. A., Newsom, H. E., Landheim, R., & McKay, C. P. (1999). Hydrogeologic
 726 evolution of gale crater and its relevance to the exobiological exploration of mars. *Icarus*,
 727 *139*(2), 235–245. doi: 10.1006/icar.1999.6099
- 728 Cardenas, B. T., & Lamb, M. P. (2022, October). Paleogeographic reconstructions of an ocean mar-
 729 gin on mars based on deltaic sedimentology at aeolis dorsa. *Journal of Geophysical Research:*
 730 *Planets*, *127*(10). doi: 10.1029/2022je007390

- 731 Cardenas, B. T., Lamb, M. P., & Grotzinger, J. P. (2022, October). Martian landscapes of fluvial
732 ridges carved from ancient sedimentary basin fill. *Nature Geoscience*, *15*(11), 871–877. doi:
733 10.1038/s41561-022-01058-2
- 734 Cardenas, B. T., Mohrig, D., & Goudge, T. A. (2017, 09). Fluvial stratigraphy of valley fills at
735 Aeolis Dorsa, Mars: Evidence for base-level fluctuations controlled by a downstream water
736 body. *GSA Bulletin*, *130*(3-4), 484–498. doi: 10.1130/B31567.1
- 737 Craddock, R. A., Maxwell, T. A., & Howard, A. D. (1997). Crater morphometry and modification
738 in the sinus sabaeus and margaritifer sinus regions of mars. *Journal of Geophysical Research:*
739 *Planets*, *102*(E6), 13321–13340. doi: 10.1029/97JE01084
- 740 Day, M., Edgett, K. S., & Stumbaugh, D. (2019, December). Ancient stratigraphy preserving a
741 wet-to-dry, fluvio-lacustrine to aeolian transition near barth crater, arabia terra, mars. *Journal*
742 *of Geophysical Research: Planets*, *124*(12), 3402–3421. Retrieved from [https://doi](https://doi.org/10.1029/2019je006226)
743 [.org/10.1029/2019je006226](https://doi.org/10.1029/2019je006226) doi: 10.1029/2019je006226
- 744 Dong, T. Y., & Goudge, T. A. (2022, 06). Quantitative relationships between river and channel-belt
745 planform patterns. *Geology*, *50*(9), 1053–1057. doi: 10.1130/G49935.1
- 746 Dong, T. Y., Nittrouer, J. A., Czapiga, M. J., Ma, H., McElroy, B., Il'icheva, E., . . . Parker, G. (2019,
747 January). Roles of Bank Material in Setting Bankfull Hydraulic Geometry as Informed by the
748 Selenga River Delta, Russia. *Water Resources Research*, *55*(1), 827–846. doi: 10.1029/
749 2017WR021985
- 750 Dunne, K. B. J., & Jerolmack, D. J. (2018). Evidence of, and a proposed explanation for, bimodal
751 transport states in alluvial rivers. *Earth Surface Dynamics*, *6*(3), 583–594. doi: 10.5194/
752 esurf-6-583-2018
- 753 Dunne, K. B. J., & Jerolmack, D. J. (2020). What sets river width? *Science Advances*, *6*(41),
754 eabc1505. doi: 10.1126/sciadv.abc1505
- 755 Edmonds, D. A., & Slingerland, R. L. (2010, February). Significant effect of sediment cohesion on
756 delta morphology. *Nature Geoscience*, *3*(2), 105–109. doi: 10.1038/ngeo730
- 757 Edwards, M. B., & Eri, K. A. (1983). Paleochannel geometry and flow patterns determined from
758 exhumed permian point bars in north-central texas. *SEPM Journal of Sedimentary Research*,
759 *Vol. 53*. doi: 10.1306/212f835a-2b24-11d7-8648000102c1865d
- 760 Fassett, C. I. (2016). Analysis of impact crater populations and the geochronology of planetary
761 surfaces in the inner solar system. *Journal of Geophysical Research: Planets*, *121*(10), 1900–
762 1926. doi: 10.1002/2016JE005094
- 763 Fassett, C. I., & Head, J. W. (2008, May). The timing of martian valley network activity: Constraints
764 from buffered crater counting. *Icarus*, *195*(1), 61–89. doi: 10.1016/j.icarus.2007.12.009
- 765 Fassett, C. I., & Head III, J. W. (2005). Fluvial sedimentary deposits on mars: Ancient deltas in
766 a crater lake in the nili fossae region. *Geophysical Research Letters*, *32*(14). doi: 10.1029/
767 2005GL023456
- 768 Forsberg-Taylor, N. K., Howard, A. D., & Craddock, R. A. (2004). Crater degradation in the
769 martian highlands: Morphometric analysis of the sinus sabaeus region and simulation mod-
770 eling suggest fluvial processes. *Journal of Geophysical Research: Planets*, *109*(E5). doi:
771 10.1029/2004JE002242
- 772 Frazier, D. E. (1967). Recent deltaic deposits of the Mississippi River: their development and
773 chronology. *Transactions of the Gulf Coast Association of Geological Societies*, *27*, 287–
774 315.
- 775 Ganti, V., Straub, K. M., Foufoula-Georgiou, E., & Paola, C. (2011). Space-time dynamics of de-
776 positional systems: Experimental evidence and theoretical modeling of heavy-tailed statistics.
777 *Journal of Geophysical Research: Earth Surface*, *116*(F2). doi: 10.1029/2010JF001893
- 778 Golombek, M., Robinson, K., McEwen, A., Bridges, N., Ivanov, B., Tornabene, L., & Sullivan,

- 779 R. (2010). Constraints on ripple migration at meridiani planum from opportunity and hirise
780 observations of fresh craters. *Journal of Geophysical Research: Planets*, *115*(E7). doi: 10
781 .1029/2010JE003628
- 782 Golombek, M. P., Grant, J. A., Crumpler, L. S., Greeley, R., Arvidson, R. E., Bell III, J. F., ...
783 Squyres, S. W. (2006). Erosion rates at the mars exploration rover landing sites and long-
784 term climate change on mars. *Journal of Geophysical Research: Planets*, *111*(E12). doi:
785 10.1029/2006JE002754
- 786 Golombek, M. P., Warner, N. H., Ganti, V., Lamb, M. P., Parker, T. J., Fergason, R. L., & Sullivan,
787 R. (2014). Small crater modification on meridiani planum and implications for erosion rates
788 and climate change on mars. *Journal of Geophysical Research: Planets*, *119*(12), 2522–2547.
789 doi: 10.1002/2014JE004658
- 790 Goudge, T. A., Mohrig, D., Cardenas, B. T., Hughes, C. M., & Fassett, C. I. (2018, February).
791 Stratigraphy and paleohydrology of delta channel deposits, jezero crater, mars. *Icarus*, *301*,
792 58–75. Retrieved from <https://doi.org/10.1016/j.icarus.2017.09.034>
793 doi: 10.1016/j.icarus.2017.09.034
- 794 Grotzinger, J., Arvidson, R., Bell, J., Calvin, W., Clark, B., Fike, D., ... Watters, W. (2005).
795 Stratigraphy and sedimentology of a dry to wet eolian depositional system, burns formation,
796 meridiani planum, mars. *Earth and Planetary Science Letters*, *240*(1), 11–72. doi: 10.1016/
797 j.epsl.2005.09.039
- 798 Grotzinger, J. P., Gupta, S., Malin, M. C., Rubin, D. M., Schieber, J., Siebach, K., ... Wilson, S. A.
799 (2015, October). Deposition, exhumation, and paleoclimate of an ancient lake deposit, gale
800 crater, mars. *Science*, *350*(6257). doi: 10.1126/science.aac7575
- 801 Hajek, E. A., & Edmonds, D. A. (2014, March). Is river avulsion style controlled by floodplain
802 morphodynamics? *Geology*, *42*(3), 199–202. doi: 10.1130/G35045.1
- 803 Hajek, E. A., & Straub, K. M. (2017). Autogenic sedimentation in clastic stratigraphy. *Annual*
804 *Review of Earth and Planetary Sciences*, *45*(1), 681–709. doi: 10.1146/annurev-earth-063016
805 -015935
- 806 Hariharan, J., Passalacqua, P., Xu, Z., Michael, H. A., Steel, E., Chadwick, A., ... Moodie, A. J.
807 (2022). Modeling the dynamic response of river deltas to sea-level rise acceleration. *Journal*
808 *of Geophysical Research: Earth Surface*, *127*(9). doi: 10.1029/2022JF006762
- 809 Hariharan, J., Wright, K., Moodie, A., Tull, N., & Passalacqua, P. (2023). Impacts of human
810 modifications on material transport in deltas. *Earth Surface Dynamics*, *11*(3), 405–427. doi:
811 10.5194/esurf-11-405-2023
- 812 Hariharan, J., Xu, Z., Michael, H. A., Paola, C., Steel, E., & Passalacqua, P. (2021, August). Linking
813 the surface and subsurface in river deltas—part 1: Relating surface and subsurface geometries.
814 *Water Resources Research*, *57*(8). doi: 10.1029/2020wr029282
- 815 Hartmann, W. K. (1966). Martian cratering. *Icarus*, *5*(1), 565–576. doi: 10.1016/0019-1035(66)
816 90071-6
- 817 Hartmann, W. K. (1971). Martian cratering iii: Theory of crater obliteration. *Icarus*, *15*(3), 410–
818 428. doi: 10.1016/0019-1035(71)90119-9
- 819 Hartmann, W. K., & Neukum, G. (2001). Cratering chronology and the evolution of mars. *Space*
820 *Science Reviews*, *96*(1/4), 165–194. doi: 10.1023/a:1011945222010
- 821 Hayden, A. T., Lamb, M. P., Fischer, W. W., Ewing, R. C., McElroy, B. J., & Williams, R. M.
822 (2019). Formation of sinuous ridges by inversion of river-channel belts in utah, usa, with
823 implications for mars. *Icarus*, *332*, 92–110. doi: 10.1016/j.icarus.2019.04.019
- 824 Herkenhoff, K. E., & Plaut, J. J. (2000). Surface ages and resurfacing rates of the polar layered
825 deposits on mars. *Icarus*, *144*(2), 243–253. doi: 10.1006/icar.1999.6287
- 826 Hiesinger, H., Head III, J. W., Wolf, U., Jaumann, R., & Neukum, G. (2002). Lunar mare basalt

- 827 flow units: Thicknesses determined from crater size-frequency distributions. *Geophysical*
 828 *Research Letters*, 29(8), 89-1–89-4. doi: 10.1029/2002GL014847
- 829 Hoke, M. R. T., & Hynek, B. M. (2009, August). Roaming zones of precipitation on ancient mars
 830 as recorded in valley networks. *Journal of Geophysical Research: Planets*, 114(E8). doi:
 831 10.1029/2008je003247
- 832 Howard, A. (2004). Simple non-fluvial models of planetary surface modification, with application
 833 to mars. In *Lunar and planetary science conference* (p. 1054).
- 834 Howard, A. D. (2007). Simulating the development of martian highland landscapes through the
 835 interaction of impact cratering, fluvial erosion, and variable hydrologic forcing. *Geomorphol-*
 836 *ogy*, 91(3), 332–363. doi: 10.1016/j.geomorph.2007.04.017
- 837 Irwin, R. P., Lewis, K. W., Howard, A. D., & Grant, J. A. (2015, July). Paleohydrology of eber-
 838 swalde crater, mars. *Geomorphology*, 240, 83–101. Retrieved from [https://doi.org/](https://doi.org/10.1016/j.geomorph.2014.10.012)
 839 [10.1016/j.geomorph.2014.10.012](https://doi.org/10.1016/j.geomorph.2014.10.012) doi: 10.1016/j.geomorph.2014.10.012
- 840 Irwin, R. P., Tanaka, K. L., & Robbins, S. J. (2013, February). Distribution of early, middle,
 841 and late noachian cratered surfaces in the martian highlands: Implications for resurfacing
 842 events and processes. *Journal of Geophysical Research: Planets*, 118(2), 278–291. doi:
 843 10.1002/jgre.20053
- 844 Ivanov, B. A. (2001). Mars/moon cratering rate ratio estimates. *Space Science Reviews*, 96(1/4),
 845 87–104. doi: 10.1023/a:1011941121102
- 846 Jerolmack, D. J., & Paola, C. (2007, November). Complexity in a cellular model of river avulsion.
 847 *Geomorphology*, 91(3-4), 259–270. doi: 10.1016/j.geomorph.2007.04.022
- 848 Jerolmack, D. J., & Sadler, P. (2007). Transience and persistence in the depositional record of
 849 continental margins. *Journal of Geophysical Research: Earth Surface*, 112(F3). doi: 10.1029/
 850 2006JF000555
- 851 Kim, W., Petter, A., Straub, K., & Mohrig, D. (2014, August). Investigating the autogenic process
 852 response to allogenic forcing: experimental geomorphology and stratigraphy. In A. W. Mar-
 853 tinius, R. Ravnås, J. A. Howell, R. J. Steel, & J. P. Wonham (Eds.), *From Depositional Systems*
 854 *to Sedimentary Successions on the Norwegian Continental Margin* (pp. 127–138). Chichester,
 855 UK: John Wiley & Sons, Ltd. doi: 10.1002/9781118920435.ch5
- 856 Kite, E. S. (2019, January). Geologic constraints on early mars climate. *Space Science Reviews*,
 857 215(1). doi: 10.1007/s11214-018-0575-5
- 858 Kite, E. S., Lucas, A., & Fassett, C. I. (2013). Pacing early mars river activity: Embedded craters
 859 in the aeolis dorsa region imply river activity spanned $\geq(1-20)$ myr. *Icarus*, 225(1), 850–855.
 860 doi: 10.1016/j.icarus.2013.03.029
- 861 Kite, E. S., Mischna, M. A., Fan, B., Morgan, A. M., Wilson, S. A., & Richardson, M. I. (2022,
 862 May). Changing spatial distribution of water flow charts major change in mars's greenhouse
 863 effect. *Science Advances*, 8(21). Retrieved from [https://doi.org/10.1126/sciadv](https://doi.org/10.1126/sciadv.abo5894)
 864 [.abo5894](https://doi.org/10.1126/sciadv.abo5894) doi: 10.1126/sciadv.abo5894
- 865 Kite, E. S., Williams, J.-P., Lucas, A., & Aharonson, O. (2014, April). Low palaeopressure of the
 866 martian atmosphere estimated from the size distribution of ancient craters. *Nature Geoscience*,
 867 7(5), 335–339. doi: 10.1038/ngeo2137
- 868 Lapôtre, M. G. A., & Ielpi, A. (2020). The pace of fluvial meanders on mars and implications for the
 869 western delta deposits of jezero crater. *AGU Advances*, 1(2). doi: 10.1029/2019AV000141
- 870 Lauzon, R., & Murray, A. B. (2018). Comparing the cohesive effects of mud and vegetation
 871 on delta evolution. *Geophysical Research Letters*, 45(19), 10,437-10,445. doi: 10.1029/
 872 2018GL079405
- 873 Lauzon, R., Piliouras, A., & Rowland, J. C. (2019, June). Ice and permafrost effects on delta mor-
 874 phology and channel dynamics. *Geophysical Research Letters*. doi: 10.1029/2019GL082792

- 875 Leeder, M. (1978). A Quantitative Stratigraphic Model for Alluvium, with Special Reference to
876 Channel Deposit Density and Interconnectedness. *Fluvial Sedimentology, Memoir 5*, 587–
877 596.
- 878 Lewis, K. W., & Aharonson, O. (2014, June). Occurrence and origin of rhythmic sedimentary
879 rocks on mars. *Journal of Geophysical Research: Planets*, *119*(6), 1432–1457. doi: 10.1002/
880 2013je004404
- 881 Liang, M., Geleynse, N., Edmonds, D. A., & Passalacqua, P. (2015b, January). A reduced-
882 complexity model for river delta formation – Part 2: Assessment of the flow routing scheme.
883 *Earth Surface Dynamics*, *3*(1), 87–104. doi: 10.5194/esurf-3-87-2015
- 884 Liang, M., Van Dyk, C., & Passalacqua, P. (2016, February). Quantifying the patterns and dynamics
885 of river deltas under conditions of steady forcing and relative sea level rise: QUANTIFYING
886 DELTA PATTERNS AND DYNAMICS. *Journal of Geophysical Research: Earth Surface*,
887 *121*(2), 465–496. doi: 10.1002/2015JF003653
- 888 Liang, M., Voller, V. R., & Paola, C. (2015a, January). A reduced-complexity model for river delta
889 formation – Part 1: Modeling deltas with channel dynamics. *Earth Surface Dynamics*, *3*(1),
890 67–86. doi: 10.5194/esurf-3-67-2015
- 891 Limaye, A. B. S., & Lamb, M. P. (2013). A vector-based method for bank-material tracking in
892 coupled models of meandering and landscape evolution. *Journal of Geophysical Research:*
893 *Earth Surface*, *118*(4), 2421–2437. doi: <https://doi.org/10.1002/2013JF002854>
- 894 Malin, M. C., & Edgett, K. S. (2000). Sedimentary rocks of early mars. *Science*, *290*(5498),
895 1927–1937. doi: 10.1126/science.290.5498.1927
- 896 Mangold, N., Adeli, S., Conway, S., Ansan, V., & Langlais, B. (2012, April). A chronology of early
897 mars climatic evolution from impact crater degradation. *Journal of Geophysical Research:*
898 *Planets*, *117*(E4). doi: 10.1029/2011je004005
- 899 Matsubara, Y., Howard, A. D., & Irwin, R. P. (2018, November). Constraints on the noachian paleo-
900 climate of the martian highlands from landscape evolution modeling. *Journal of Geophysical*
901 *Research: Planets*, *123*(11), 2958–2979. doi: 10.1029/2018je005572
- 902 McEwen, A. S., Eliason, E. M., Bergstrom, J. W., Bridges, N. T., Hansen, C. J., Delamere, W. A.,
903 ... Weitz, C. M. (2007). Mars reconnaissance orbiter's high resolution imaging science
904 experiment (hirise). *Journal of Geophysical Research: Planets*, *112*(E5). doi: 10.1029/
905 2005JE002605
- 906 Melosh, H. J. (1989). *Impact cratering : a geologic process*. New York, NY: Oxford University
907 Press.
- 908 Michael, G. (2013). Planetary surface dating from crater size–frequency distribution measurements:
909 Multiple resurfacing episodes and differential isochron fitting. *Icarus*, *226*(1), 885–890. doi:
910 10.1016/j.icarus.2013.07.004
- 911 Michael, G., Kneissl, T., & Neesemann, A. (2016). Planetary surface dating from crater size-
912 frequency distribution measurements: Poisson timing analysis. *Icarus*, *277*, 279–285. doi:
913 10.1016/j.icarus.2016.05.019
- 914 Milliken, R. E., Grotzinger, J. P., & Thomson, B. J. (2010). Paleoclimate of mars as captured by
915 the stratigraphic record in gale crater. *Geophysical Research Letters*, *37*(4). doi: 10.1029/
916 2009GL041870
- 917 Minton, D. A., Richardson, J. E., & Fassett, C. I. (2015). Re-examining the main asteroid belt as
918 the primary source of ancient lunar craters. *Icarus*, *247*, 172–190. doi: 10.1016/j.icarus.2014
919 .10.018
- 920 Mohrig, D., Heller, P. L., Paola, C., & Lyons, W. J. (2000). Interpreting avulsion process from
921 ancient alluvial sequences: Guadalope-Matarranya system (northern Spain) and Wasatch For-
922 mation (western Colorado). *Geological Society of America Bulletin*, *112*(12), 1787–1803.

- 923 Moodie, A. J., Hariharan, J., Barefoot, E., & Passalacqua, P. (2021). pyDeltaRCM: a flexible
 924 numerical delta model. *Journal of Open Source Software*. doi: 10.21105/joss.03398
- 925 Moodie, A. J., Nittrouer, J. A., Ma, H., Carlson, B. N., Chadwick, A. J., Lamb, M. P., & Parker,
 926 G. (2019). Modeling deltaic lobe-building cycles and channel avulsions for the yellow river
 927 delta, china. *Journal of Geophysical Research: Earth Surface*, *124*(11), 2438–2462. doi:
 928 10.1029/2019JF005220
- 929 Moodie, A. J., & Passalacqua, P. (2021). When does faulting-induced subsidence drive dis-
 930 tributary network reorganization? *Geophysical Research Letters*, *48*(22). doi: 10.1029/
 931 2021GL095053
- 932 Neukum, G., & Horn, P. (1976). Effects of lava flows on lunar crater populations. *The Moon*,
 933 *15*(3-4), 205–222. Retrieved from <https://doi.org/10.1007/bf00562238> doi:
 934 10.1007/bf00562238
- 935 Öpik, E. J. (1966). The martian surface. *Science*, *153*(3733), 255–265. doi: 10.1126/science.153
 936 .3733.255
- 937 Parker, G. (2004, November). *E-book: 1D sediment transport morphodynam-
 938 ics with applications to rivers and turbidity currents*. E-book. (Available at:
 939 http://hydrolab.illinois.edu/people/parkerg/morphodynamics_e-book.htm)
- 940 Parker, G., Paola, C., Whipple, K. X., Mohrig, D., Toro-Escobar, C. M., Halverson, M., & Skoglund,
 941 T. W. (1998, October). Alluvial Fans Formed by Channelized Fluvial and Sheet Flow. II:
 942 Application. *Journal of Hydraulic Engineering*, *124*(10), 996–1004. doi: 10.1061/(ASCE)
 943 0733-9429(1998)124:10(996)
- 944 Pike, R. J. (1977, January). Size-dependence in the shape of fresh impact craters on the moon. In
 945 D. J. Roddy, R. O. Pepin, & R. B. Merrill (Eds.), *Impact and explosion cratering: Planetary
 946 and terrestrial implications* (pp. 489–509).
- 947 Piliouras, A., Lauzon, R., & Rowland, J. C. (2021). Unraveling the combined effects of ice and
 948 permafrost on arctic delta morphodynamics. *Journal of Geophysical Research: Earth Surface*,
 949 *126*(4). doi: 10.1029/2020JF005706
- 950 Popova, O., Nemtchinov, I., & Hartmann, W. K. (2003, June). Bolides in the present and past
 951 martian atmosphere and effects on cratering processes. *Meteoritics & Planetary Science*,
 952 *38*(6), 905–925. doi: 10.1111/j.1945-5100.2003.tb00287.x
- 953 Reitz, M. D., & Jerolmack, D. J. (2012, May). Experimental alluvial fan evolution: Channel
 954 dynamics, slope controls, and shoreline growth. *Journal of Geophysical Research*, *117*(F2).
 955 doi: 10.1029/2011JF002261
- 956 Reitz, M. D., Jerolmack, D. J., & Swenson, J. B. (2010, March). Flooding and flow path selection
 957 on alluvial fans and deltas: FLOW PATH SELECTION ON ALLUVIAL FANS. *Geophysical
 958 Research Letters*, *37*(6), n/a–n/a. doi: 10.1029/2009GL041985
- 959 Richardson, J. E. (2009). Cratering saturation and equilibrium: A new model looks at an old
 960 problem. *Icarus*, *204*(2), 697–715. doi: 10.1016/j.icarus.2009.07.029
- 961 Richardson, J. E., Melosh, H. J., & Greenberg, R. (2004). Impact-induced seismic activity on
 962 asteroid 433 eros: A surface modification process. *Science*, *306*(5701), 1526–1529. doi:
 963 10.1126/science.1104731
- 964 Richardson, J. E., Melosh, H. J., Greenberg, R. J., & O'Brien, D. P. (2005). The global effects
 965 of impact-induced seismic activity on fractured asteroid surface morphology. *Icarus*, *179*(2),
 966 325–349. doi: 10.1016/j.icarus.2005.07.005
- 967 Robbins, S. J., & Hynek, B. M. (2012). A new global database of mars impact craters ≥ 1 km: 2.
 968 global crater properties and regional variations of the simple-to-complex transition diameter.
 969 *Journal of Geophysical Research: Planets*, *117*(E6). doi: 10.1029/2011JE003967
- 970 Ross, H. P. (1968). A simplified mathematical model for lunar crater erosion. *Journal of Geophysical*

- 971 *Research (1896-1977)*, 73(4), 1343–1354. doi: 10.1029/JB073i004p01343
- 972 Russ, J. C. (1986). *Practical stereology*. Springer US. doi: 10.1007/978-1-4899-3533-5
- 973 Sadler, P. M. (1981). Sediment accumulation rates and the completeness of stratigraphic sections.
974 *The Journal of Geology*, 89(5), 569–584. doi: 10.1086/628623
- 975 Schultz, P. H., & Gault, D. E. (1975, January). Seismically induced modification of lunar surface
976 features. *Lunar and Planetary Science Conference Proceedings*, 3, 2845–2862.
- 977 Schumer, R., Jerolmack, D., & McElroy, B. (2011). The stratigraphic filter and bias in measurement
978 of geologic rates. *Geophysical Research Letters*, 38(11). doi: 10.1029/2011GL047118
- 979 Schumm, S. A. (1985). Patterns of alluvial rivers. *Annual Review of Earth and Planetary Sciences*,
980 13(1), 5–27. doi: 10.1146/annurev.ea.13.050185.000253
- 981 Slingerland, R., & Smith, N. D. (2004, May). RIVER AVULSIONS AND THEIR DEPOSITS.
982 *Annual Review of Earth and Planetary Sciences*, 32(1), 257–285. doi: 10.1146/annurev.earth
983 .32.101802.120201
- 984 Smith, M. R., Gillespie, A. R., & Montgomery, D. R. (2008). Effect of obliteration on crater-
985 count chronologies for martian surfaces. *Geophysical Research Letters*, 35(10). doi: 10.1029/
986 2008GL033538
- 987 Smith, N. D., Cross, T. A., Dufficy, J. P., & Clough, S. R. (1989, February). Anatomy of an avulsion.
988 *Sedimentology*, 36(1), 1–23. doi: 10.1111/j.1365-3091.1989.tb00817.x
- 989 Soderblom, L. A. (1970). A model for small-impact erosion applied to the lunar surface. *Journal of*
990 *Geophysical Research (1896-1977)*, 75(14), 2655–2661. doi: 10.1029/JB075i014p02655
- 991 Stack-Morgan, K. M., Gupta, S., Tebolt, M., Caravaca, G., Ives, L. R., Russell, P., ... Williams,
992 R. M. (2023). Sedimentology and stratigraphy of the lower delta sequence, jezero crater, mars.
993 The Woodlands, TX, USA. Retrieved from [https://ntrs.nasa.gov/citations/
994 20230000582](https://ntrs.nasa.gov/citations/20230000582)
- 995 Straub, K. M., Duller, R. A., Foreman, B. Z., & Hajek, E. A. (2020). Buffered, incomplete, and
996 shredded: The challenges of reading an imperfect stratigraphic record. *Journal of Geophysical*
997 *Research: Earth Surface*, 125(3). doi: 10.1029/2019JF005079
- 998 Straub, K. M., & Esposito, C. R. (2013). Influence of water and sediment supply on the stratigraphic
999 record of alluvial fans and deltas: Process controls on stratigraphic completeness. *Journal of*
1000 *Geophysical Research: Earth Surface*, 118(2), 625–637. doi: 10.1002/jgrf.20061
- 1001 Straub, K. M., Li, Q., & Benson, W. M. (2015). Influence of sediment cohesion on deltaic shoreline
1002 dynamics and bulk sediment retention: A laboratory study. *Geophysical Research Letters*,
1003 42(22), 9808–9815. doi: 10.1002/2015GL066131
- 1004 Straub, K. M., Paola, C., Mohrig, D., Wolinsky, M. A., & George, T. (2009, 09). Compensational
1005 Stacking of Channelized Sedimentary Deposits. *Journal of Sedimentary Research*, 79(9),
1006 673–688. doi: 10.2110/jsr.2009.070
- 1007 Stucky de Quay, G., Goudge, T. A., Kite, E. S., Fassett, C. I., & Guzewich, S. D. (2021, August).
1008 Limits on runoff episode duration for early mars: Integrating lake hydrology and climate
1009 models. *Geophysical Research Letters*, 48(15). doi: 10.1029/2021gl093523
- 1010 Tejedor, A., Schwenk, J., Kleinhans, M., Limaye, A. B., Vulis, L., Carling, P., ... Fofoula-
1011 Georgiou, E. (2022, August). The entropic braiding index (ebi): A robust metric to account for
1012 the diversity of channel scales in multi-thread rivers. *Geophysical Research Letters*, 49(16).
1013 doi: 10.1029/2022gl099681
- 1014 Trampush, S. M., Huzurbazar, S., & McElroy, B. (2014). Empirical assessment of theory for
1015 bankfull characteristics of alluvial channels. *Water Resources Research*, 50(12), 9211–9220.
1016 doi: 10.1002/2014WR015597
- 1017 Wang, Y., Straub, K. M., & Hajek, E. A. (2011, 09). Scale-dependent compensational stacking:
1018 An estimate of autogenic time scales in channelized sedimentary deposits. *Geology*, 39(9),

- 1019 811–814. doi: 10.1130/G32068.1
- 1020 Warren, A. O., Kite, E. S., Williams, J.-P., & Horgan, B. (2019). Through the thick and thin: New
1021 constraints on mars paleopressure history 3.8–4 ga from small exhumed craters. *Journal of*
1022 *Geophysical Research: Planets*, 124(11), 2793–2818. doi: 10.1029/2019JE006178
- 1023 Wells, N. A., & Dorr, J. A. (1987). Shifting of the Kosi River, northern India. *Geology*, 15(3), 204.
1024 doi: 10.1130/0091-7613(1987)15(\$204:SOTKRN\$)2.0.CO;2
- 1025 Wickert, A. D., Martin, J. M., Tal, M., Kim, W., Sheets, B., & Paola, C. (2013, June). River
1026 channel lateral mobility: metrics, time scales, and controls: RIVER CHANNEL LATERAL
1027 MOBILITY. *Journal of Geophysical Research: Earth Surface*, 118(2), 396–412. doi: 10
1028 .1029/2012JF002386
- 1029 Williams, J.-P., Pathare, A. V., & Aharonson, O. (2014). The production of small primary craters
1030 on mars and the moon. *Icarus*, 235, 23–36. doi: 10.1016/j.icarus.2014.03.011
- 1031 Williams, J.-P., van der Bogert, C. H., Pathare, A. V., Michael, G. G., Kirchoff, M. R., & Hiesinger,
1032 H. (2018). Dating very young planetary surfaces from crater statistics: A review of issues and
1033 challenges. *Meteoritics & Planetary Science*, 53(4), 554–582. doi: 10.1111/maps.12924
- 1034 Wolman, M. G., & Miller, J. P. (1960, January). Magnitude and Frequency of Forces in Geomorphic
1035 Processes. *The Journal of Geology*, 68(1), 54–74. doi: 10.1086/626637
- 1036 Woronow, A. (1977). Crater saturation and equilibrium: A monte carlo simulation. *Journal of*
1037 *Geophysical Research (1896-1977)*, 82(17), 2447–2456. doi: 10.1029/JB082i017p02447
- 1038 Woronow, A. (1978). A general cratering-history model and its implications for the lunar highlands.
1039 *Icarus*, 34(1), 76–88. doi: 10.1016/0019-1035(78)90127-6
- 1040 Wright, K., Hariharan, J., Passalacqua, P., Salter, G., & Lamb, M. P. (2022). From grains to plas-
1041 tics: Modeling nourishment patterns and hydraulic sorting of fluvially transported materials
1042 in deltas. *Journal of Geophysical Research: Earth Surface*, 127(11), e2022JF006769. doi:
1043 10.1029/2022JF006769
- 1044 Yielding, G., Needham, T., & Jones, H. (1996). Sampling of fault populations using sub-surface
1045 data: a review. *Journal of Structural Geology*, 18(2), 135–146. doi: 10.1016/S0191-8141(96)
1046 80039-3

Supporting Information for:
**Fluvial reworking eliminates small craters, but does not
meaningfully bias the Mars interbedded-crater record**

Andrew J. Moodie^{1,2} and Timothy A. Goudge²

¹Department of Geography, Texas A&M University

²Department of Earth and Planetary Sciences, The University of Texas at Austin

Contents of this file

1. Text S1
2. Figures S1 to S6

S1. Supplementary Materials

S1.1. Model implementation notes

The gravitational constant (g) enters the delta model by controlling a weighting parameter (γ) that balances water routing between topographic and inertial mechanisms. We elected not to modify this weighting from the Earth-based -9.81 m/s^2 , because changing the gravitational constant has almost no impact on the weighting parameter, and therefore is unlikely to have any meaningful impact on the delta model behavior if adjusted to Mars gravity. For example, where $g = 9.81$, the balancing parameter $\gamma = 0.01308$, and for $g = 3.71$, the balancing parameter $\gamma = 0.004946667$; so either 98.7% dependent on inertial routing rules, or 99.5% dependent on inertial routing rules. We note that systematically changing the weighting parameter in DeltaRCM has not previously been examined.

A recent study demonstrates how sediment suspensions and therefore total sediment transport may be enhanced under reduced Mars gravity (Braat et al., 2023), but gravity does not impact sediment suspension or transport in the model. It may be possible to modify routing rules for sand and mud in the DeltaRCM framework to represent this enhanced suspension; for example, following interpretations of the θ parameter as a proxy for vertical material stratification (Hariharan et al., 2020; Wright et al., 2022).

Because this is a rules-based reduced-complexity model (and not actual physics that depend on the gravitational constant), and because we are studying how channel dynamics and craters interact to a first order, we decided not to vary either γ or θ in model simulations.

S1.2. Crater preservation metrics in detail

We performed additional analyses and metric calculations of crater reworking that were not included in the main text (Figure S1). Overall, these additional analyses confirm that the model is working as expected, and that study conclusions cannot be attributed to another process.

We first compared the diameter of craters determined as interbedded versus those not identified as being interbedded (Figure S1a), to validate that our automatic labeling of interbedded craters was not imparting any size-dependent bias on the crater record. We identify no difference between the diameters of the interbedded craters and non-interbedded craters; or specifically, we cannot reject the null hypothesis that the distributions are from the same population in a two-sample t-test ($p=0.68$). Subsequent analyses and figures in this section include only interbedded craters.

Next, we assess the potential for a time bias to explain observations of crater preservation, in essence, testing alternative hypothesis that preservation is controlled mostly by the time a crater was formed and more recently formed craters will be better preserved; note that time here is cast as elapsed model seconds, which according to the model intermittency formulation scales linearly to the 1, 10, and 100 Myr crater accumulation timescales. Figure S1b shows that there is a slight tendency for the very oldest craters to be less preserved than craters throughout the rest of the simulation. But, in gross, there is not a clear relationship between crater rim fraction preserved and model simulation time. We additionally investigated whether a time-based preservation bias existed in the data at all by considering only preservation at the delta landform surface at the end of simulation (Figure S1c). Indeed, older craters are less preserved at the delta surface; this is indicative of both burial by sediment over time (i.e., preservation in stratigraphy) and fluvial reworking of sediments at the surface. Interestingly, comparing rim fraction preserved at the sediment surface to crater diameter (Figure S1d) reveals a pattern similar to the

overall preservation metric from the main text (Figure 5a). Together, these patterns suggest that the model and analyses are working as expected: creating interbedded craters that are either buried or reworked (or both) over time.

Another facet of the data to examine was whether crater position on the delta affected preservation. Figure S1e shows that the distance from the inlet channel a crater formed has no influence on the preservation of that crater. Consistent with the notion of a deltaic landform that grows over time, there is a (noisy) decrease in age of craters with increasing distance from the inlet (apparent from the broad purple-to-green-to-yellow shift from left to right in Figure S1e).

We examined whether there was any trend in preservation as it related to the elevation of the sediment surface (i.e., the land or bottom of shallow sea) upon which the crater formed (Figure S1f); this elevation is termed the reference elevation (Howard, 2007). Here, the data also record the expected pattern of a delta growing over time, with higher reference elevations occurring only later in elapsed model time. Importantly though, there is no discernible relationship between reference elevation and rim fraction preserved (Figure S1f), indicating that this is not a factor biasing interbedded crater size-frequency distributions.

To understand the correlation we between rim fraction preserved and preserved rim continuity, we examined how these metrics compared for each interbedded crater (Figure S1g). As expected, metrics are clearly correlated, though the rim fraction preserved is (with very few exceptions) higher than the commensurate preserved rim continuity, on a normalized basis (e.g., 0.5 commensurate with 180°). This asymmetry arises because preserved rim continuity is a more strict metric, in the sense that narrow breaks in rim continuity immediately lower the metric, but fraction preserved can still be high.

Finally, we display the timeseries of crater sizes (aggregated across all simulations to demonstrate that cratering is treated as a Poisson process, with arrival times (i.e., crater production times) independent of all other events (Figure S1h).

S1.3. Cumulative distribution sensitivities

We examined the sensitivity of crater-size cumulative distributions to various steps in our workflow. Figure S2 shows how fluvial reworking-biased distributions, as well as distributions biased by fluvial reworking and exhumation, vary when extracted for a single simulation with duration 1, 10, or 100 Myr, and are characterized by a smaller number of craters (11 craters, rather than 56). To generate these distributions (Figure S2), we randomly selected a single simulation from each simulation-duration ensemble, then followed the same analysis routine as in the main text. In short, to characterize fluvial reworking bias, we first randomly select 11 interbedded craters from the simulation, then exclude those craters with $<180^\circ$ rim continuity, and repeat this process 100 times to assess distribution variability; we show the median distribution as a solid line, and 16th to 84th percentile distributions as a shaded envelope. We then characterize exhumation bias by applying an increased weighting probability for larger craters to be sampled, whereby probability of a crater with diameter d to be included in the synthetic distribution goes as $p(d) \propto d/d_{min}$, where $d_{min} \approx 10$ m is the smallest crater diameter in the simulations.

With the exception of the 1 Myr duration simulation (Figure S2a), cumulative distributions generated for individual simulations are similar to the aggregated simulation results (Figure 6). In the 1 Myr case (Figure S2a), the crater size distribution is narrow and ranges 10–30 m diameter craters, such that the sampled distributions deviate from the distribution of all interbedded craters. In the 10 Myr case (Figure S2b), fluvial reworking leads to enhanced bias and increased

variability with respect to the aggregated simulation results (Figure 6), though the median distribution does not scale similarly to observed crater size-frequency distributions on Mars. In the 100 Myr case (Figure S2c), the results are effectively identical to the aggregated simulation results (i.e., Figure 6), but with a larger amount of variability here that arises due to the small sample size (11 craters sampled, rather than 56). The total number of interbedded craters in a single 1 Myr duration simulation (10–33) is substantially fewer than a 100 Myr duration simulation (1625–2894), such that cumulative distributions generated from a single 1 Myr duration simulation are especially susceptible to small number effects. Importantly, even in the extreme cases of small number statistics demonstrated here, no sampled distributions reproduce observed crater size-frequency distributions on Mars.

Additionally, we examined how cumulative distributions made from the aggregated simulation results are modulated by the selected rim continuity threshold, the number of craters observed in the crater record, and exhumational bias (Figure S3). In this part of the sensitivity analysis, we follow the same workflow as in the main text but isolated one component of the workflow to vary, and calculated *only the combined effect* of fluvial reworking and exhumational bias for visual clarity in figures; all figures show the median distribution as a solid line, and 16th to 84th percentile distributions as a shaded envelope.

In the main text, we use a rim continuity threshold of 180° to determine which interbedded craters are mappable, so we varied this threshold from 60° to 310° here (Figure S3a). There is some variation in median distributions, but the envelope of variability in the distributions is overlapping, leading us to conclude there is little difference in the outcome of our study with selection of a different rim continuity threshold. Though we do not robustly validate this idea, we suspect that the limited variability arises from the fact that distributions are dominated by smaller craters (≤ 50 m) that are less than a channel width in diameter, and so are often either completely removed or completely preserved, and therefore contribute equally cumulative distributions when the rim continuity threshold is varied 60°–310°. Additionally, spatial discretization of crater deposits creates discrete quanta for preservation metrics of smaller craters, because there are only 8 cells that make up the crater rim (see main text and Section S1.5); this also potentially limits the impact of the selected rim continuity threshold.

In the main text, we use 56 craters from the interbedded crater record to generate cumulative distribution functions and compare with the Mars crater record (i.e., Figure 6), so varied the number of craters selected in generating cumulative distributions from 24 to 88 here (Figure S3b). Distribution medians and envelopes of variability are indistinguishable from one another, indicating that this choice has little effect on results. Note that, when selecting only 11 craters from a single 1 Myr simulation (Figure S2a) it is possible to modulate crater size cumulative distributions. However, for values that can reasonably be considered representative samples ($n=24$ to 88; Figure S3b), the number of samples does not affect the interpretation that fluvial reworking and exhumation bias cannot explain the observed record.

In the main text, we represent exhumation bias as an increased observation probability based on crater diameter. We attempted to validate the theory underlying this proportional scaling in the course of our research, and determined that it likely provides an acceptable first-order approximation of the effect; we discuss this empirical validation, and opportunities for further research briefly in the main text (Section 4.4.3), and in more detail below in Section S1.6. Here, we demonstrate possible distributions that could be generated by various proportionalities of exhumational bias. We selected exponents l from 0.5 to 2.5, that modify the proportionality as $p(d) \propto d^l / d_{min}$ (Figure S3c); $l = 1$ is the default proportionality and is used throughout the

main text. Exhumational bias has the largest impact on CSFDs of all threshold sensitivities examined. But, even in the most extreme case of $l = 2.5$, exhumational bias cannot reproduce observed crater records. Notably, in our empirical testing of exhumational bias, we determined that an exhumational bias proportional to the diameter squared (d^2) yields an exponent k of -1.2 , consistent with the bias of smallest craters observed in the slow aggradation simulation. It is not clear to us whether increased exhumational bias (e.g., $\propto d^2$) in combination with fluvial reworking and other uncertain degradation processes, might meaningfully modulate cumulative crater size distributions. This will be an important area for future research, and could be achieved with a landscape evolution model simulating erosional exhumation of craters embedded in heterogeneous sedimentary volumes (e.g., Cardenas et al., 2022).

S1.4. Effect of crater obliteration on metrics and conclusions

We quantified the effect of crater obliteration, that is, the destruction of an existing crater when a new crater is formed, on metrics used in our analyses. This process is implicitly included in our simulations, and we want to understand the magnitude of crater removal due to obliteration, relative to fluvial reworking. To quantify the effect, we ran nine simulations without river-delta sediment input, and generated craters according to the same routine as the main text. In these sensitivity test simulations, the synthesized crater size-frequency distribution was consistent with the Ivanov (2001) production function, and the Hartmann and Neukum (2001) Mars chronology function for 100 Myr of elapsed time beginning 3.5 Ga (e.g., Figure 2).

We calculated the rim fraction preserved, ejecta fraction preserved, and preserved rim continuity in the same way as the main text (Figure S4). It is well known that crater obliteration leads to a size-dependent bias that preferentially eliminates smaller craters from the crater record (Woronow, 1977, 1978; Smith et al., 2008; Richardson, 2009; Minton et al., 2015). Our sensitivity testing reveals the same observation, with all three crater preservation metrics showing a preferential removal of smaller craters (Figure S4). Notably, 25 m-bin averages indicate that the average effect of crater obliteration is smaller than the fluvial reworking effect (i.e., Figure 5). Importantly, this sensitivity test is an overestimate of the magnitude of the crater obliteration effect in the main text simulations. In main text simulations, craters can be incorporated into the stratigraphic record over time, and therefore move away from the sediment surface and are less susceptible to overprinting by subsequent craters.

S1.5. Space and time discretization effects

Our model and analysis are executed on a rectilinear grid, which leads to spatial and temporal discretization effects. Spatial discretization effects are introduced to our workflow at two critical points: first, when craters are created on the model grid, and second when we convert a model elevation timeseries to a stratigraphic volume. Temporal discretization is introduced into our workflow during model simulation, because model state is only intermittently recorded (not continuously). Here, we consider the potential impact of these effects on our results. Importantly, we determine that study conclusions are not affected by spatial and temporal discretization, though precise values of reworking may be sensitive to vertical discretization.

Figure S5a shows the spatially discretized topography along a transect through the center of craters with varying diameters. Although crater depressions consistently become wider with increasing diameter, the maximum height does not monotonically increase due to discretization. Note, that this effect is fairly minor (a few meters difference for a 60 versus 80 m diameter crater), and that there is an overall trend of increasing maximum rim height

Discretized rim height is less than analytical rim height for modeled crater sizes $\lesssim 100$ m, and drops to a constant value of 0.2 m for craters < 10 m in diameter (Figure S5b). For these smallest crater diameters, the distance from crater center to rim is less than one half grid cell width, so the rim is not effectively rendered on the grid. During simulation, rims of craters in this diameter range likely present very little of a vertical obstruction to flow. Thus, discretization could lead to a small overestimate of reworking of the smallest fraction of crater sizes in our study, but we do not expect this could explain or meaningfully impact the overall trends and conclusions of our study. We did not examine the effect of vertical or horizontal spatial discretization in detail for this article.

Temporal discretization arises because not every iteration of the numerical delta model is written to file. Therefore, there is potential that crater rims and ejecta are reworked by either fluvial processes or by obliteration during formation of new craters. In any case, the potential bias from temporal discretization is minimized by saving model state to the output file frequently (Hariharan et al., 2021). We quantified the effect of crater obliteration through a record of craters representing 100 Myr elapsed time, and the effect is relatively minor as compared to fluvial reworking (Section S1.4). Channels occupy a small fraction of the overall delta area at any point in time, so it seems unlikely a large number of craters would be reworked before recorded. Given these facts, we do not expect that temporal discretization has any impact on trends and conclusions identified in our study.

S1.6. Exhumation bias proportionality

Exhumational bias is the interacting set of processes that preferentially expose larger craters when a sedimentary volume with interbedded craters is eroded (Kite et al., 2013). Stereological theory underpins exhumational bias (Russ, 1986; Yielding et al., 1996); in short, the likelihood of a plane through a three-dimensional volume intersecting an object embedded in the volume depends on the object length-scale in the axis normal to the plane. For an erosional surface that cuts a quasi-horizontal plane through a sedimentary volume with embedded craters, the likelihood a crater is exposed on the plane therefore depends on the crater depth. Assuming a semi-hemispherical crater shape fixes the ratio between crater diameter and depth (e.g., Melosh, 1989), and therefore makes exhumational probability proportional to crater diameter (Kite et al., 2014; Warren et al., 2019; Lewis & Aharonson, 2014). However, this framework assumes that 1) the largest crater depths are small with respect to the sedimentary volume thickness, 2) that erosional surfaces are reasonably approximated by planes, and 3) that proportionality of exhuming crater deposits (i.e., rim and ejecta material) is the same as the probability of exhuming the bowl-like depression of a crater. Our study accepted these assumptions, but sensitivity testing indicates that further scrutiny of this geometry-based exhumational bias model is needed.

We attempted to empirically validate the exhumational bias relevant to our study (i.e., exhumed crater rim deposits), by modeling crater rim and ejecta deposits randomly embedded in a stratigraphic volume and subsequently exhumed along a horizontal plane. To do so, we created a set of model runs with the same parameterizations as 100 Myr simulations, but with a broader range of craters generated ranging 10–1000 m in diameter, and with sediment accumulation set to be constant and uniform over the model domain; in essence, we turn off fluvial-deltaic sedimentation and impose burial at a specified vertical rate. We examined the effect of a fast (1 m/Myr) and a slow (0.06 m/Myr) sediment accumulation rate, which correspond to sediment thicknesses of 100 m and 6 m, respectively; 6 m is approximately the thickness of deposits modeled in this study. After simulation, we randomly selected 51 horizontal planes from the

stratigraphic volume, and identified crater rim deposits that intersected with the plane (emphasis: only crater rim deposits were counted), and repeated this analysis on a second replicate simulation for each of fast and slow aggradation. Similar to analysis in our study, this routine assumes that exhumation does not degrade craters, but only exposes or completely eliminates them from the record, and is affected by crater obliteration during formation of new craters (like simulations in the main text). Finally, we fit an exponent k to the recovered crater size-frequency distributions consistent with an imposed power-law CSFD (e.g., Hartmann, 2005).

These tests indicate that a sampling probability proportional to crater diameter is a conservative (i.e., lower-bound) estimate of the exhumational bias effect (Figure S6). The exponent fit to the full crater size-frequency distribution is -3 , which is consistent with the expectation from crater production functions (Hartmann, 2005). When sampling proportional to diameter (i.e., exactly as we do in the main text), we find the fit exponent is -2 , which is consistent with the theory (Lewis & Aharonson, 2014). When empirically sampling the idealized sedimentary volumes via intersection with random horizontal planes, we find the fit exponent is -1.6 and -1.2 for the fast and slow aggradation volumes, respectively. That is, sampling bias is more extreme in both empirical tests than in proportional sampling, and potentially largest in slow-aggradation environments.

In the fast aggradation case where the sedimentary volume reaches 100 m in thickness, the best-fit exponent of the power law appears to reasonably explain the individual observed sets of craters (Figure S6). This is in contrast to the trend between individual sets of craters empirically sampled from the slow aggradation case, and the best-fit exponent. Looking in detail at the slow aggradation case, the sampled distributions follow closely with the full crater size-frequency distribution for crater diameters $\gtrsim 40$ m, and diverge considerably over smaller crater diameters (Figure S6). That is, larger crater rim deposits are *nearly always* sampled by exhumation bias when the deposit thickness is low, but there is only a chance that smaller crater rim deposits are sampled thereby imparting a bias. The best-fit coefficient may therefore be erroneous for this slow-aggradation case, but bias among smaller craters is consistent with the faster aggradation case and different from the probabilistic exhumation (i.e., > -2).

We note that in empirical sampling, we tested for intersection with crater rim deposits and not the bowl-like depression of a crater. There is no easy way to test for the latter in our modeling approach, so we did not separate the effect on the exponent of what is intersected and aggradation rate. Though, if aggradation rate did not also have some effect, there would be no difference between fast and slow tests.

In sum, we do not expect that even the most extreme plausible exhumation bias determined by these experiments would favor larger craters so significantly that our results would change. It will be an interesting topic for future modeling studies to explore how crater deposits are morphodynamically exhumed from sedimentary strata, and therefore examine exhumational bias in greater detail.

References

- Braat, L., Brückner, M., Sefton-Nash, E., & Lamb, M. (2023, April). Gravity-driven differences in fluvial sediment transport fluxes on mars and earth. *none*. Retrieved from <https://doi.org/10.31223/x5bq0r> doi: 10.31223/x5bq0r
- Cardenas, B. T., Lamb, M. P., & Grotzinger, J. P. (2022, October). Martian landscapes of fluvial ridges carved from ancient sedimentary basin fill. *Nature Geoscience*, *15*(11), 871–877. doi: 10.1038/s41561-022-01058-2
- Hariharan, J., Wright, K., & Passalacqua, P. (2020, October). dorado: A python package for simulating passive particle transport in shallow-water flows. *Journal of Open Source Software*, *5*(54), 2585. doi: 10.21105/joss.02585
- Hariharan, J., Xu, Z., Michael, H. A., Paola, C., Steel, E., & Passalacqua, P. (2021, August). Linking the surface and subsurface in river deltas—part 1: Relating surface and subsurface geometries. *Water Resources Research*, *57*(8). doi: 10.1029/2020wr029282
- Hartmann, W. K. (2005). Martian cratering 8: Isochron refinement and the chronology of mars. *Icarus*, *174*(2), 294–320. doi: 10.1016/j.icarus.2004.11.023
- Hartmann, W. K., & Neukum, G. (2001). Cratering chronology and the evolution of mars. *Space Science Reviews*, *96*(1/4), 165–194. doi: 10.1023/a:1011945222010
- Howard, A. D. (2007). Simulating the development of martian highland landscapes through the interaction of impact cratering, fluvial erosion, and variable hydrologic forcing. *Geomorphology*, *91*(3), 332–363. doi: 10.1016/j.geomorph.2007.04.017
- Ivanov, B. A. (2001). Mars/moon cratering rate ratio estimates. *Space Science Reviews*, *96*(1/4), 87–104. doi: 10.1023/a:1011941121102
- Kite, E. S., Lucas, A., & Fassett, C. I. (2013). Pacing early mars river activity: Embedded craters in the aeolis dorsa region imply river activity spanned $\geq(1-20)$ myr. *Icarus*, *225*(1), 850–855. doi: 10.1016/j.icarus.2013.03.029
- Kite, E. S., Williams, J.-P., Lucas, A., & Aharonson, O. (2014, April). Low palaeopressure of the martian atmosphere estimated from the size distribution of ancient craters. *Nature Geoscience*, *7*(5), 335–339. doi: 10.1038/ngeo2137
- Lewis, K. W., & Aharonson, O. (2014, June). Occurrence and origin of rhythmic sedimentary rocks on mars. *Journal of Geophysical Research: Planets*, *119*(6), 1432–1457. doi: 10.1002/2013je004404
- Melosh, H. J. (1989). *Impact cratering : a geologic process*. New York, NY: Oxford University Press.
- Minton, D. A., Richardson, J. E., & Fassett, C. I. (2015). Re-examining the main asteroid belt as the primary source of ancient lunar craters. *Icarus*, *247*, 172–190. doi: 10.1016/j.icarus.2014.10.018
- Richardson, J. E. (2009). Cratering saturation and equilibrium: A new model looks at an old problem. *Icarus*, *204*(2), 697–715. doi: 10.1016/j.icarus.2009.07.029
- Russ, J. C. (1986). *Practical stereology*. Springer US. doi: 10.1007/978-1-4899-3533-5
- Smith, M. R., Gillespie, A. R., & Montgomery, D. R. (2008). Effect of obliteration on crater-

- count chronologies for martian surfaces. *Geophysical Research Letters*, 35(10). doi: 10.1029/2008GL033538
- Warren, A. O., Kite, E. S., Williams, J.-P., & Horgan, B. (2019). Through the thick and thin: New constraints on mars paleopressure history 3.8–4 ga from small exhumed craters. *Journal of Geophysical Research: Planets*, 124(11), 2793–2818. doi: 10.1029/2019JE006178
- Woronow, A. (1977). Crater saturation and equilibrium: A monte carlo simulation. *Journal of Geophysical Research (1896-1977)*, 82(17), 2447–2456. doi: 10.1029/JB082i017p02447
- Woronow, A. (1978). A general cratering-history model and its implications for the lunar highlands. *Icarus*, 34(1), 76–88. doi: 10.1016/0019-1035(78)90127-6
- Wright, K., Hariharan, J., Passalacqua, P., Salter, G., & Lamb, M. P. (2022). From grains to plastics: Modeling nourishment patterns and hydraulic sorting of fluvially transported materials in deltas. *Journal of Geophysical Research: Earth Surface*, 127(11). doi: 10.1029/2022JF006769
- Yielding, G., Needham, T., & Jones, H. (1996). Sampling of fault populations using sub-surface data: a review. *Journal of Structural Geology*, 18(2), 135–146. doi: 10.1016/S0191-8141(96)80039-3

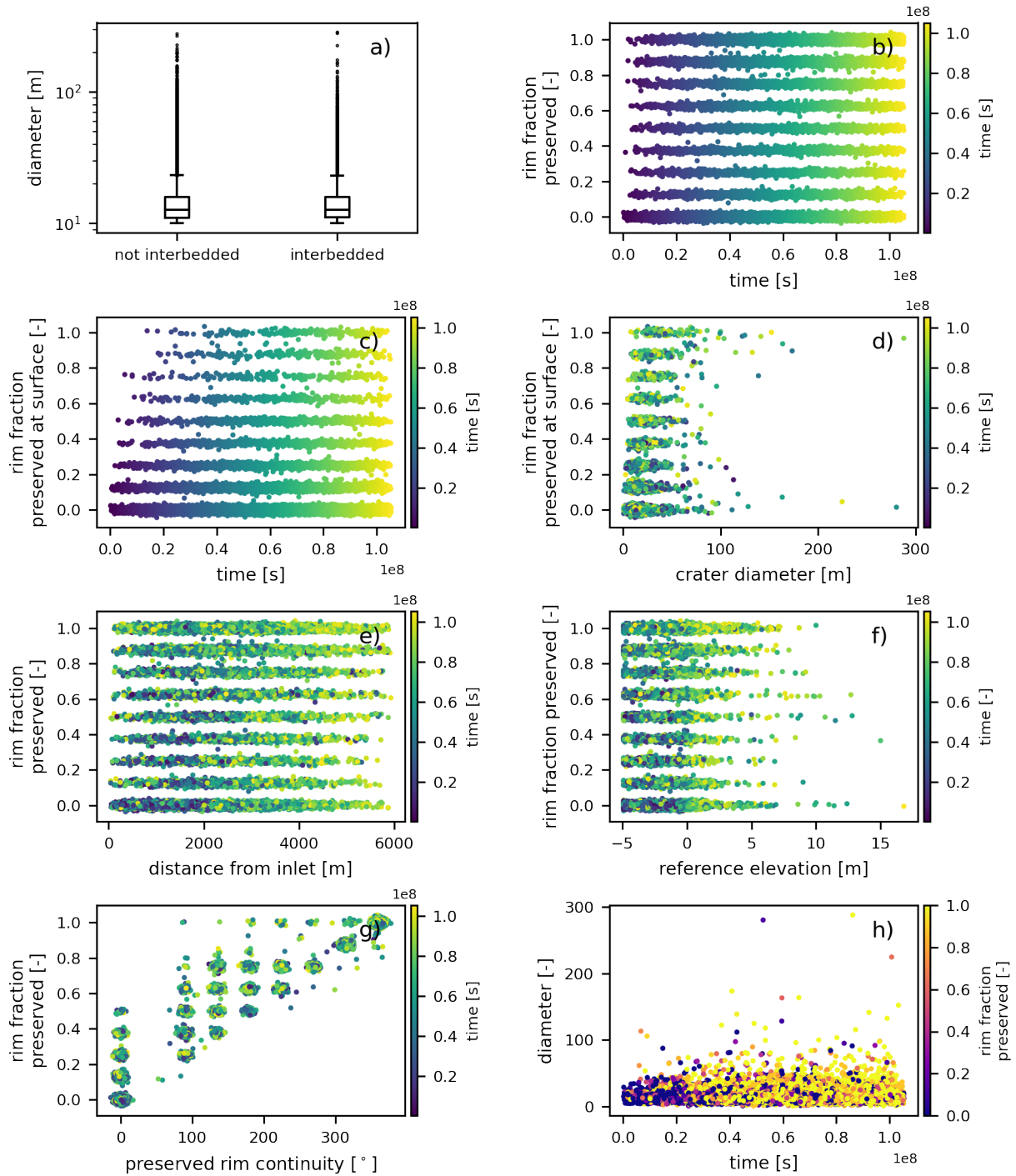


Figure S1. Additional assessments of crater preservation metrics. Overall, these analyses indicate that the delta model and crater analysis scripts are working as expected. See Section S1.2 for an interpretation of each panel.

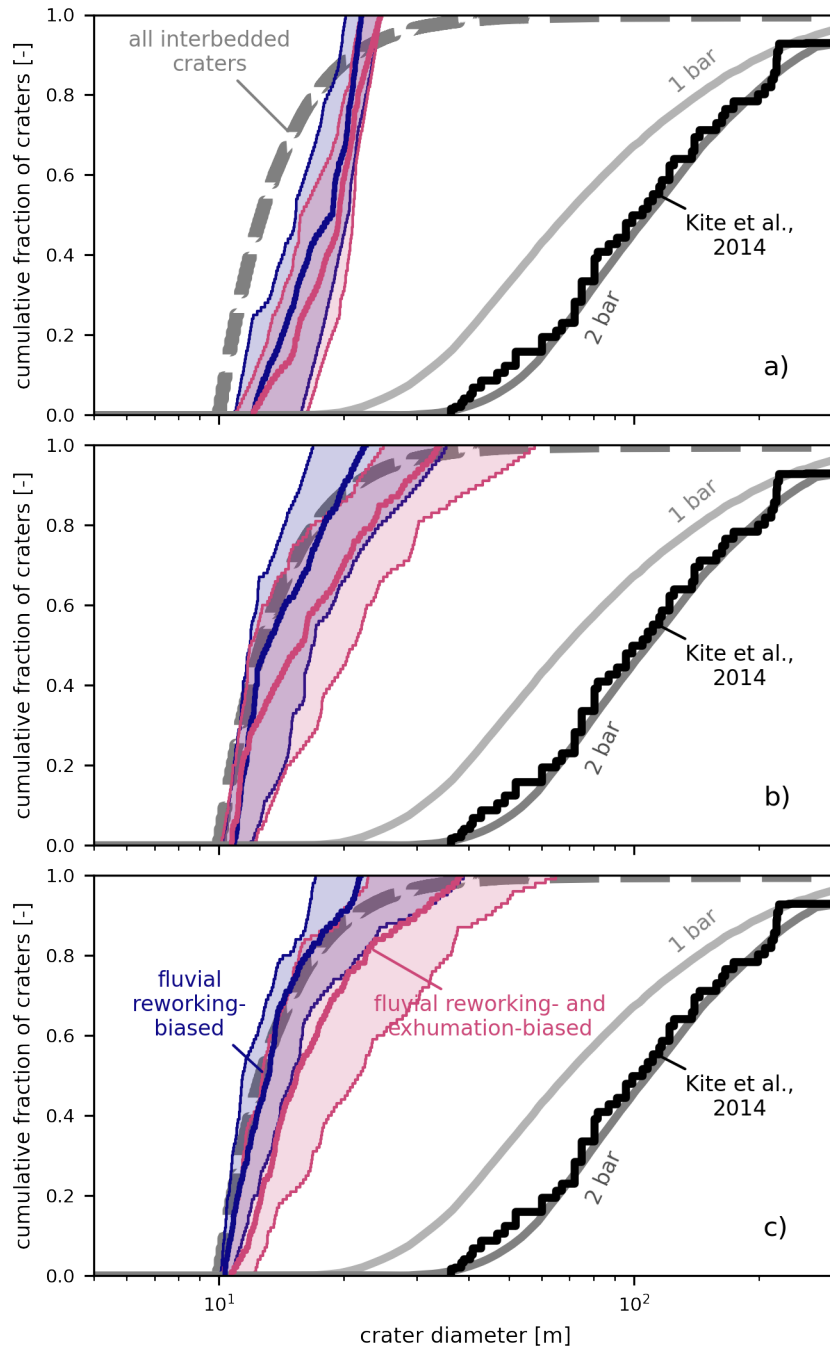


Figure S2. Cumulative distributions generated for a single simulation from the ensemble of each simulation duration, a) 1, b) 10, and c) 100 Myr. Only in the extreme case of fast deposition (1 Myr), it is possible to modify the distribution position, but even in this case, bias does not cause distribution to scale similarly to observed Mars interbedded crater record. Distributions were generated using only 11 crater samples (in contrast to 56 used in the main text) and repeated 100 times to assess distribution variability; figures show the median distribution as a solid line, and 16th to 84th percentile distribution as a shaded envelope.

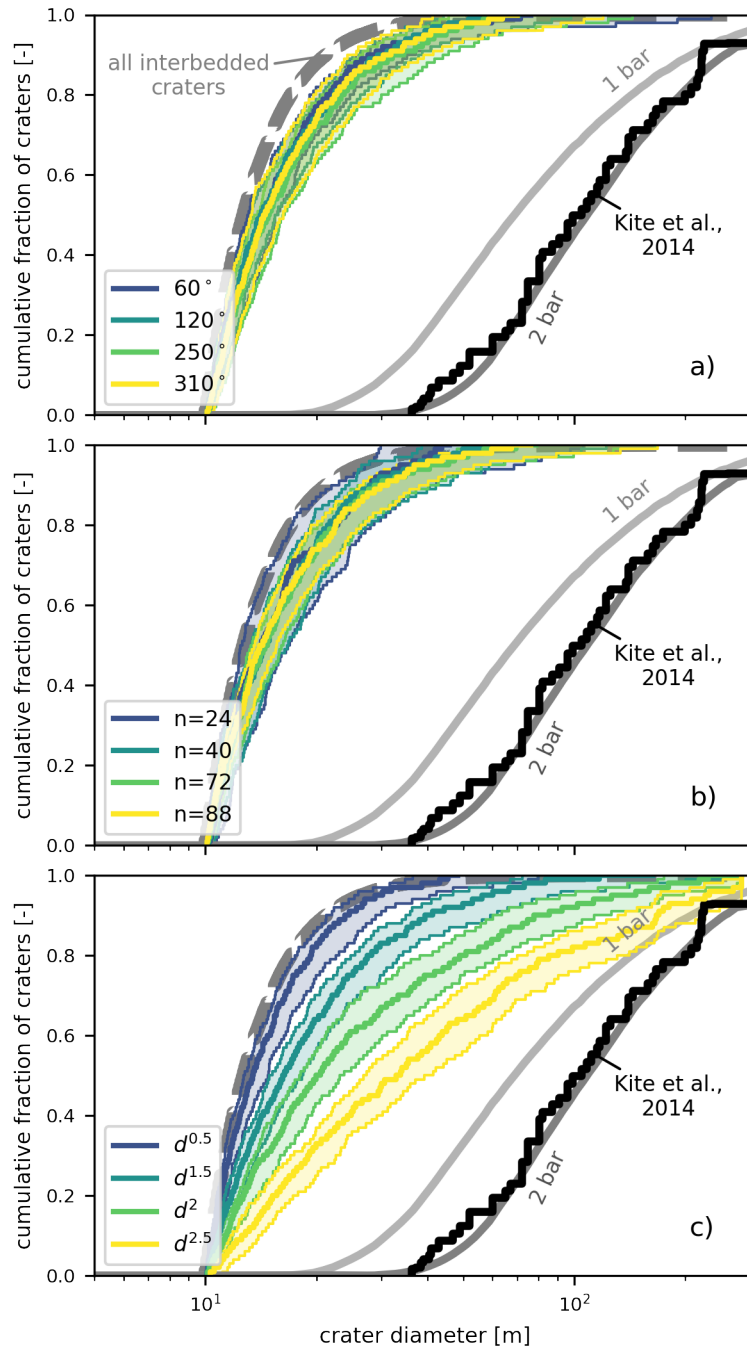


Figure S3. Cumulative crater size-frequency distributions generated for different parameter values used to threshold and modify data distributions in our workflow. a) Distributions generated for various rim continuity thresholds ranging from 60° to 310° (default is 180° , used throughout the main text). b) Distributions generated for various number of craters selected to include in the distributions ranging from 24 to 88 (default is 56, used throughout the main text). c) Distributions generated for various exhumation proportionalities with respect to crater diameter d , with proportionalities ranging 0.5 to 2.5 (default is 1, used throughout the main text).

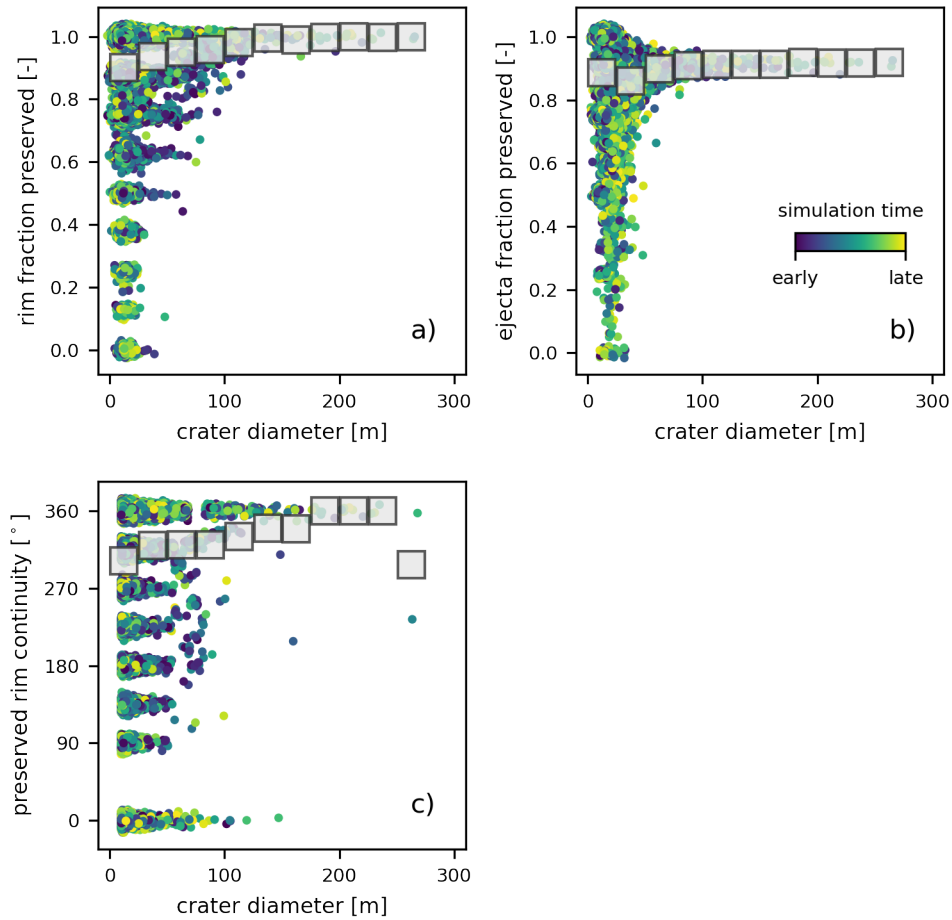


Figure S4. a) Rim fraction preserved, b) ejecta fraction preserved, and c) preserved rim continuity as a function of crater diameter for replicate simulations with no input sediment, to test crater obliteration by formation of new craters. Individual craters are colored by crater formation time within a simulation and have normally-distributed noise added for visualization to both axes (mean is 0, and standard deviation is ± 0.01 or $\pm 1.5^\circ$, and ± 1.5 m), and gray boxes mark non-overlapping 25 m-bin averages. Smaller craters ($\lesssim 50$ m) are obliterated more often than larger craters, which creates a smaller-crater bias in the crater record; notably, the magnitude of this bias is substantially reduced with respect to fluvial reworking bias (e.g., Figure 5).

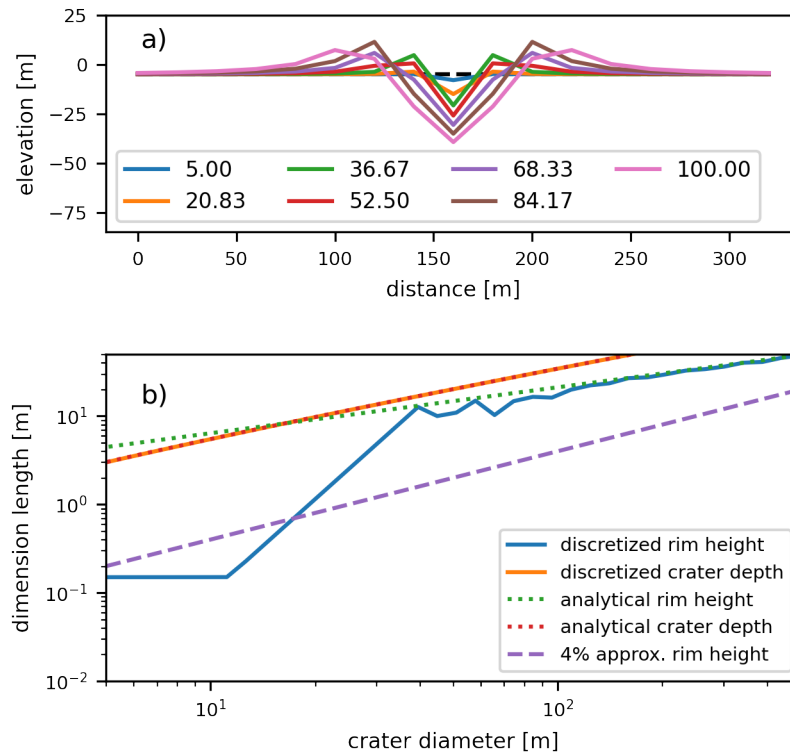


Figure S5. a) Topography of a transect through center of various diameter craters, as discretized to the model grid. b) Evaluation of crater discretized crater geometry compared to analytical geometry. Maximum crater rim height non-monotonically increases with increasing crater diameter. Discretized rim height is less than analytical rim height for modeled crater sizes $\lesssim 100$ m.

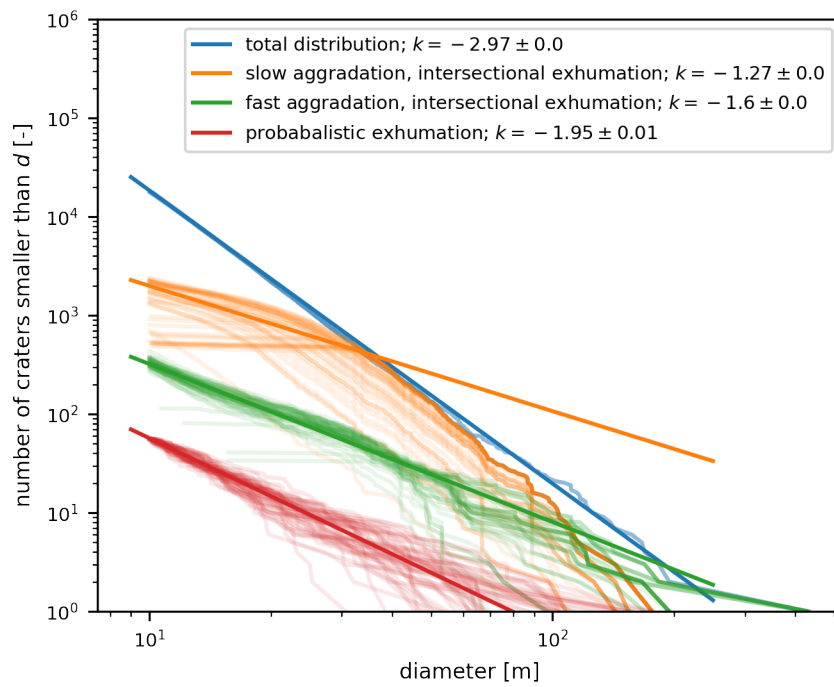


Figure S6. Crater size-frequency distributions generated from various empirical tests of potential exhumational bias. See text for more information.